Focal seizures are organized by feedback between neural activity and ion concentration changes

Damiano Gentiletti,[1] Marco de Curtis,[2] Vadym Gnatkovsky,[2,3] and Piotr Suffczynski,[1*]

Author affiliations:

1 Department of Biomedical Physics, Faculty of Physics, University of Warsaw, 02-093 Warsaw, Poland

2 Epilepsy Unit, Fondazione IRCCS Istituto Neurologico *Carlo Besta*, 20133 Milan, Italy

3 Department of Epileptology, University Hospital Bonn, 53127 Bonn, Germany

[*]Corresponding author: suffa@fuw.edu.pl

Abstract

Human and animal EEG data demonstrate that focal seizures start with low-voltage fast activity, evolve into rhythmic burst discharges and are followed by a period of suppressed background activity. This suggests that processes with dynamics in the range of tens of seconds govern focal seizure evolution. We investigate the processes associated with seizure dynamics by complementing the Hodgkin-Huxley mathematical model with the physical laws that dictate ion movement and maintain ionic gradients. Our biophysically realistic computational model closely replicates the electrographic pattern of a typical human focal seizure characterized by low voltage fast activity onset, tonic phase, clonic phase and postictal suppression. Our study demonstrates, for the first time *in silico*, the potential mechanism of seizure initiation by inhibitory interneurons via the initial build-up of extracellular K^+ due to intense interneuronal spiking. The model also identifies ionic mechanisms that may underlie a key feature in seizure dynamics, i.e., progressive slowing down of ictal discharges towards the end of seizure. Our model prediction of specific scaling of inter-burst intervals is confirmed by seizure data recorded

in the whole guinea pig brain in vitro and in humans, suggesting that the observed termination pattern may hold across different species. Our results emphasize ionic dynamics as elementary processes behind seizure generation and indicate targets for new therapeutic strategies.

Introduction

Focal seizure patterns recorded with intracranial and intracerebral electrodes in patients submitted to presurgical evaluation often consist of distinct phases (Franaszczuk et al., 1998; Spencer et al., 1992; Velascol et al., 2000). A frequently observed onset pattern in patients with temporal lobe epilepsy (TLE) is characterized by low-voltage fast (LVF) activity in the gamma range (30–80 Hz) (Avoli et al., 2016; de Curtis & Gnatkovsky, 2009; Lagarde et al., 2019; Perucca et al., 2014). LVF seizure onset is followed by the recruitment of irregular spiking behavior which evolves into periodic burst discharges that gradually decrease in frequency and suddenly cease. Seizures are often followed by a period of reduced EEG amplitude known as postictal EEG suppression. The traditional view on epileptic seizures is that they result from an imbalance of synaptic excitation and inhibition (Bradford, 1995; Bragin et al., 2009). It is unclear how this concept may account for the electroencephalographic complexity of TLE seizures and their characteristic progression from one phase to the next. The findings of several studies have not confirmed the role of synaptic interaction in seizure generation or progression. It has been shown that blocking synaptic transmission via a low Ca^{2+} solution led to the development of synchronized seizure-like events (SLE) in hippocampal CA1 slices (Jefferys & Haas, 1982; Yaari et al., 1983) and in the intact hippocampus (Feng & Durand, 2003). Moreover, the synchronized epileptiform activity can be recorded across two hippocampal regions separated by a mechanical lesion, without the involvement of electrochemical synaptic communication (Lian et al., 2001). Finally, in photosensitive baboons, light-induced neocortical seizure discharges were accompanied by depletion of extracellular Ca^{2+} to levels incompatible with the chemical synaptic transmission (Pumain et al., 1985). Additionally, a paradoxical increase in inhibitory cell firing and a decrease in pyramidal cell activity at seizure onset was documented in *in vitro* rodent slices (Derchansky et al., 2008; Fujiwara-Tsukamoto et al., 2007; Lévesque et al., 2016; Lillis et al., 2012; Ziburkus et al., 2006), in the *in vitro* whole guinea pig brain (Gnatkovsky et al., 2008; Uva et al., 2015), and in human and animal *in vivo* recordings (Elahian et al., 2018; Grasse et al., 2013; Miri et al., 2018; Toyoda et al., 2015; Truccolo et al., 2011). The above-mentioned studies suggest that processes at the network level related to changes in

synaptic gains cannot be the sole mechanisms that control seizure generation and progression, and that other factors must be involved in the process of ictogenesis.

Although several non-synaptic mechanisms have been proposed to influence abnormal synchronization (Blauwblomme et al., 2014; de Curtis et al., 2018; Jefferys et al., 2012; Raimondo et al., 2015), the specific mechanisms responsible for seizure induction, evolution and termination remain unclear. Specifically, the relative contribution of raised extracellular potassium (Avoli et al., 1996; Gnatkovsky et al., 2008) vs. increased intracellular chloride leading to depolarizing GABA responses (Alfonsa et al., 2015; Lillis et al., 2012) remains to be established. In the present study, we investigated the possible mechanisms of the LVF seizure pattern using a realistic computational model of the hippocampal network that included activity-dependent ion concentration changes. We based our simulations on the data recorded in the *in vitro* isolated guinea pig brain preparation because SLE in this model closely resemble human temporal lobe seizures (de Curtis et al., 2006; de Curtis & Gnatkovsky, 2009) and are initiated by enhanced firing of inhibitory interneurons (Gnatkovsky et al., 2008). We used these experimental recordings to guide our *in silico* study due to the availability of data at the network, cellular and ionic levels. A computer model showed that simulated seizures initiated via increased interneuron discharges, evolved and terminated autonomously due to activity-dependent ion concentration shifts and homeostatic mechanisms that worked continuously to restore physiological transmembrane ion levels. Our modelling results suggest a link between the seizure termination mechanism and postictal suppression state and predict a specific scaling law of inter-bursting intervals observed at the end of seizures, which was validated experimentally.

Results

The model consisted of five cells, four pyramidal neurons (PY) and a fast-spiking inhibitory interneuron (IN), arranged as a chain structure (Figure 1). The ionic dynamics of K^+, Na^+, Ca^{2+} and Cl^- were incorporated and activity-dependent changes in their concentrations were computed. Concentration changes in each extracellular or intracellular compartment were dependent on several mechanisms such as active and passive membrane currents, inhibitory synaptic GABAa currents, Na^+/K^+-pump, KCC2 cotransporter, glial K^+ buffer, Ca^{2+} pump and buffer, radial diffusion, longitudinal diffusion and volume changes. Additionally, we included

impermeant anions (A^-) with concentration-dependent volume changes and bicarbonate ions (HCO_3^-) that contributed to GABAa currents.

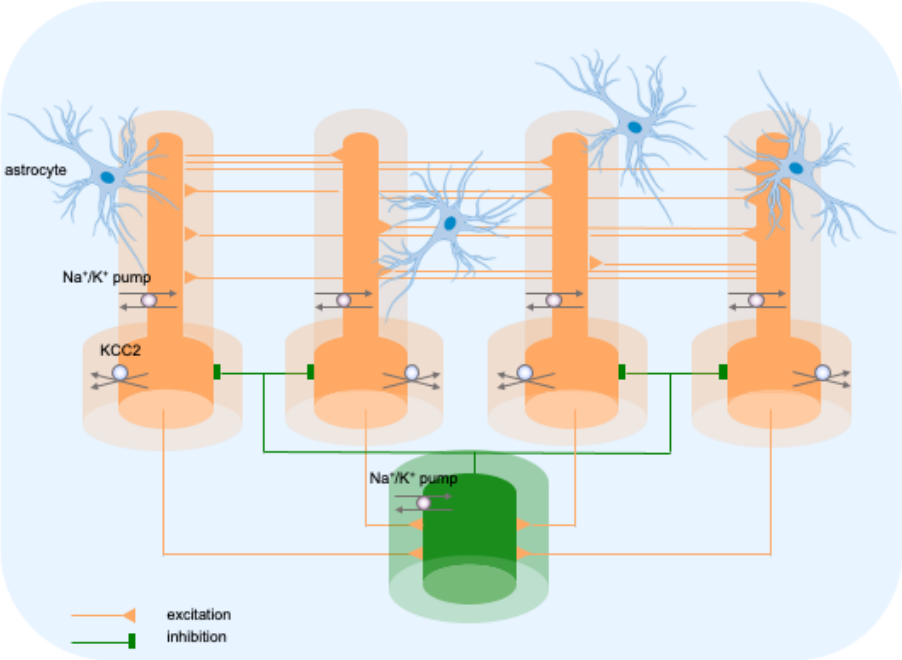

Figure 1. Model diagram. The model consisted of four pyramidal cells (orange) and an interneuron (green) linked by excitatory (AMPA) and inhibitory (GABAa) synaptic connections. Each cellular compartment was surrounded by an interstitial compartment. The interstitial space was enclosed in a common bath (blue) which represented the surrounding tissue and vasculature not included in the model. The model included variable intracellular and extracellular ion concentrations computed according to ionic currents flowing across neuronal membranes, longitudinal diffusion between the dendritic and somatic compartments, radial diffusion between neighboring interstitial compartments and diffusion to/from the bath. Additionally, the model included ionic regulation mechanisms: a Na^+/K^+-pump, a KCC2 cotransporter and K^+ buffering by astrocytes.

Three phases of an LVF onset SLE

Brief perfusions (3 minutes) of 50 microM bicuculline in the isolated guinea pig brain transiently reduces GABAergic inhibition to 60-70% and leads to strong interneuron bursting in the absence of principal cells activity (Gnatkovsky et al., 2008; Uva et al., 2015). Therefore, to initiate a SLE in the model we choose to selectively and transiently enhance discharge of the inhibitory

interneuron. In this way we made our model more general and applicable to other experimental data in which paradoxical increase in GABAergic cell firing is observed at seizure onset.

A simulated seizure emerging from normal background activity is shown in Figure 2. The SLE was triggered by depolarizing current applied to the IN at second 60 (Figure 2C, yellow trace). Strong firing (initial rate of 150 Hz) of the IN (Figure 2C) led to small amplitude fast activity in the LFP signal (Figure 2A between the 60 and 68-second timestamps) associated with the onset of the simulated SLE. After approximately 10 seconds, the PY cells began to generate a strong tonic discharge, resulting in an irregular LFP spiking signal with increased amplitude typically associated with the SLE tonic phase (Figure 2B; 65–80 seconds). Approximately 20 seconds after the onset of the SLE, the cellular firing pattern of PY cells switched from tonic to bursting discharge, leading to LFP oscillations which corresponded to the bursting phase (Figure 2A, after 80 seconds). The three types of PY cell activity are shown in an extended time scale in Appendix I – figure 1A. As the SLE progressed, the burst rate gradually decreased and ictal discharges spontaneously terminated. Postictally, the SLE was followed by a period of silence for approximately 90 seconds which was visible in the LFP signal and in the PY and IN traces (Figure 2A–C). After the postictal depression, the background firing reappeared and gradually returned to a baseline level. The SLE discharges were accompanied by significant changes in the intracellular and extracellular ionic concentrations. At the onset of the seizure, extracellular potassium concentration ($[K^+]_o$) increased sharply in the somatic compartment, remained elevated throughout the SLE and slightly decreased toward the end of the episode (Figure 2D). Intracellular sodium concentration ($[Na^+]_i$) steadily increased during the bursting phase in both somatic and dendritic compartments and reached a plateau around the offset of the SLE (Figure 2E). Intracellular chloride concentration ($[Cl^-]_i$) exhibited a gradual increase from the beginning of the SLE and was highest at the end of the paroxysmal firing (Figure 2F).

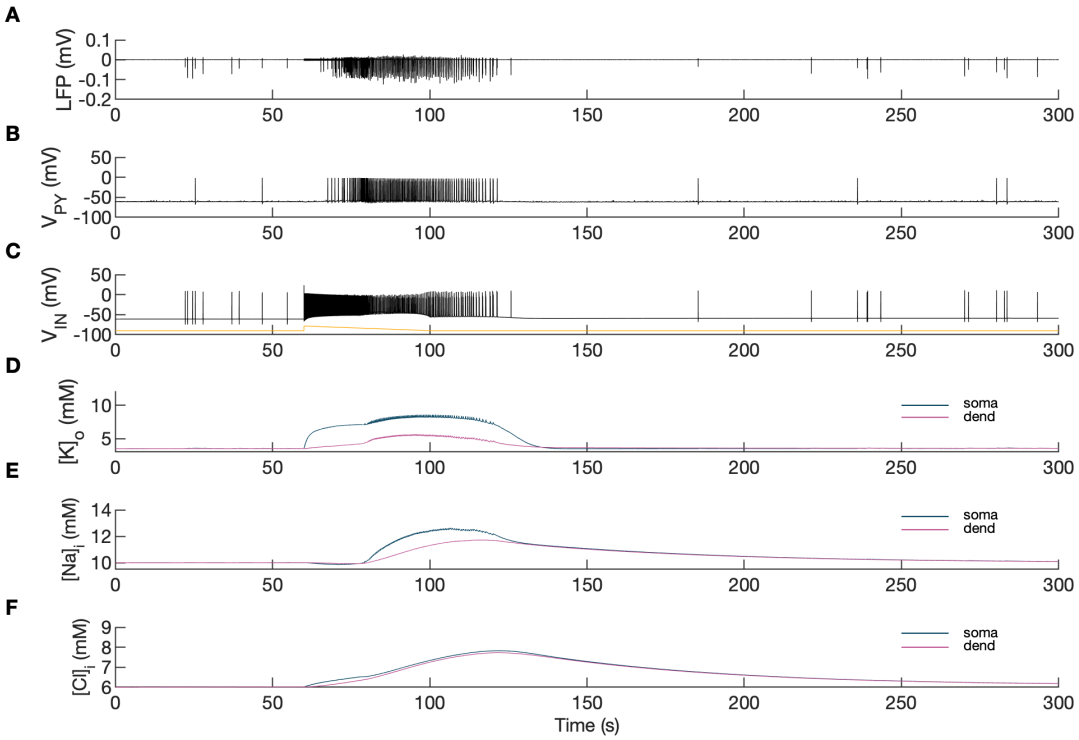

Figure 2. Model behavior during an SLE. (A) Local field potential (LFP) signal. **(B)** Pyramidal cell (PY) membrane potential. **(C)** Interneuron (IN) membrane potential. **(D)** Extracellular potassium concentration. **(E)** Intracellular sodium concentration. **(F)** Intracellular chloride concentration. In the interictal phase (0–60 seconds), the model generated irregular background firing and the ion concentrations were at their resting values (**A–F**). The current injected into the interneuron at second 60 (**C**, yellow) triggered fast IN spiking (**C**, black) which also manifested as low voltage fast activity in the LFP signal (**A**). Approximately 10 seconds after the initiation of the SLE, PY cells initiated tonic firing that subsequently shifted to bursting (**B**). The behavior of the PY cells was reflected in the LFP trace which showed irregular activity and synchronized bursting (**A**). The SLE terminated at approximately second 120 and was followed by a period of reduced excitability (**A–C**). The cellular activity was accompanied by significant ion concentration shifts. Extracellular potassium in the somatic compartment increased sharply and remained elevated throughout the SLE (**D**, dark blue). The $[K^+]_o$ increase in the dendritic compartment was slower and less pronounced (**D**, violet). The intracellular sodium increased gradually toward a plateau (**E**). The intracellular chloride accumulated steadily throughout the SLE (**F**).

A comparison of the simulation results with the available experimental data is shown in Figure 3. In the isolated guinea pig brain, the SLE activity with an LVF onset pattern (Figure

3A, top trace) was induced by 3-min arterial application of bicuculine. The transition from preictal to ictal state which occurred at approximately second 10 was associated with a strong discharge of fast-spiking interneurons (Figure 3A, third trace) and transient silencing of the PY cells (Figure 3A, second trace). Within a few seconds from the initiation of the sustained interneuron discharge, the principal PY cells were recruited first into tonic firing and subsequently into bursting discharges which were visible in the PY membrane potential and LFP signals. $[K^+]_o$ sharply increased at the onset of the SLE and remained elevated afterward (Figure 3A, bottom trace). The *in silico* results (shown for comparison in the same timescale in Figure 3B) replicated the experimental data in many respects including LFP signal characteristics, cellular firing pattern and $[K^+]_o$ time course.

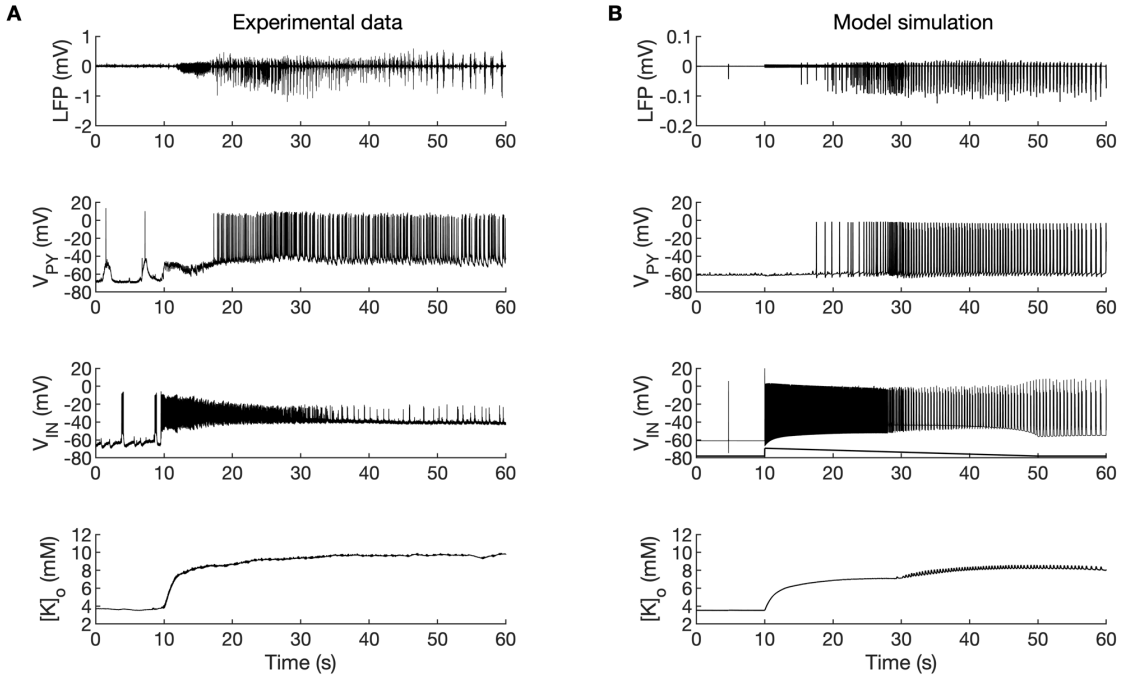

Figure 3. A comparison between the experimental data and the model simulation. (A) Experimental recordings of a seizure-like event (SLE) in the *in vitro* isolated whole guinea pig brain preparation (de Curtis et al., 2006; Gnatkovsky et al., 2008; Uva et al., 2015). From top to bottom: LFP signal, intracellular recording of the pyramidal cell (PY) and interneuron (IN), extracellular potassium. The onset of the SLE was associated with increased IN firing, silencing PY and low-voltage fast (LVF) activity in the LFP signal. Approximately 10 seconds after the onset of the SLE, the PY exhibited a tonic and then burst firing behavior. The extracellular potassium increased up to approximately 10 mM at the onset of the SLE and remained elevated

168 afterward. **(B)** The activity patterns in the LFP signal, pyramidal cells, interneuron and $[K^+]_o$
169 were reproduced accurately by the model. Signals presented in Figure 3A were recorded in
170 different experiments. LFP and interneuron data have been published previously (Gentiletti et
171 al., 2017; Gnatkovsky et al., 2008) while pyramidal cell and $[K^+]_o$ data have never been published
172 before.

173 In the simulations, the excitatory and inhibitory synaptic conductances were "clamped"
174 throughout the entire simulation period, hence, they could not contribute to the progression from
175 one phase to another. Conversely, variations in ion concentrations were expected to affect
176 neuronal excitability. For example, an increase in $[K^+]_o$ reduces the driving force of K^+ currents
177 responsible for hyperpolarized resting membrane potential and spike repolarization. $[Cl^-]_i$
178 accumulation causes depolarizing shift in E_{GABAa} reducing the efficacy of GABAa inhibition.
179 $[Na^+]_i$ and $[K^+]_o$ affect the rate of the Na^+/K^+-pump that transports three Na^+ ions out of the cell
180 for every two K^+ ions pumped into the cell, thus producing an outward current. Accumulation of
181 $[K^+]_o$ and $[Na^+]_i$ increases the pump rate and enhances the hyperpolarizing pump current. Hence,
182 to determine the intrinsic mechanism that modulates excitability, we first investigated the
183 behavior of the model in response to variations in extracellular potassium and intracellular
184 sodium concentrations and next we considered the role of chloride dynamics.

185 **The effects of $[K^+]_o$ and $[Na]_i$ on the network model**

186 Activity-dependent changes in ion concentrations are slow compared to neuronal dynamics,
187 which are relatively fast. To analyze such a system, with slow and fast timescales, it is possible
188 to decouple the fast variables (e.g., membrane potential) from the slow variables (e.g., ionic
189 concentrations). Accordingly, to analyze the role of $[K^+]_o$ and $[Na^+]_i$ in shaping single-cell and
190 network dynamics, we disabled all mechanisms controlling ionic concentrations and analyzed
191 the behavior of the model for different values of $[K^+]_o$ and $[Na^+]_i$. The values of these variables
192 were modified externally and treated as control parameters. To obtain improved affinity with the
193 reference simulation (Figure 2), the chloride concentration in the somatic and dendritic
194 compartments of the PY cells was set to 7 mM, which corresponded to its mean value during the
195 SLE (Figure 2F). In the single cell analysis, all synaptic connections were removed. In the
196 network analysis, all synaptic connections were intact except afferent excitatory input, which
197 was removed from PY cells to eliminate the stochastic component from the analysis;
198 depolarizing current injection was removed from the interneuron. The behavior of a single PY
199 cell was analyzed for different values of extracellular potassium concentration in the dendritic

200 ($[K^+]_{o,dend}$) and somatic compartments ($[K^+]_{o,soma}$). During the analysis, for each fixed value of
201 $[K^+]_{o,dend}$, we performed simulations when sweeping the $[K^+]_{o,soma}$ value from 3 mM to 12 mM
202 (in steps of 0.25 mM) in the forward and backward direction. The initial conditions for each
203 $[K^+]_{o,soma}$ value corresponded to the final states in the previous step. For each $[K^+]_{o,soma}$ step, we
204 simulated 5 seconds of activity. After a full sweep with all $[K^+]_{o,soma}$ steps in both directions, the
205 $[K^+]_{o,dend}$ was increased and the analysis was repeated. The analysis was performed for the
206 $[K^+]_{o,dend}$ values in the range of 3–6 mM, in steps of 0.5 mM (or 0.25 mM and 0.125 mM if a
207 better resolution was required). We found that the behavior of the single cell and network models
208 was the same for increasing and decreasing steps of $[K^+]_{o,soma}$ with small domains of bistability
209 not larger than one step (0.25 mM) between the activity phases. Analysis of the dynamics of a
210 single isolated cell for a reference value of $[Na^+]_i$ at 10 mM can be found in Appendix I – figure
211 1. In the network analysis, a full sweep with all $[K^+]_{o,soma}$ and $[K^+]_{o,dend}$ steps (as described above)
212 was performed for three different values of $[Na^+]_{i,soma}$ namely, 10 mM, 11 mM and 12 mM.
213 Following Figure 2E we assumed, that corresponding values of $[Na^+]_{i,dend}$ were lower and were
214 10 mM, 10.5 mM and 11 mM, respectively. The analysis results are shown in Figure 4A, in
215 which the various activity patterns, i.e., rest, tonic firing and bursting are color-coded (as shown
216 on the right). A comparison of the network activities for different values of $[Na^+]_i$ in the three
217 graphs in Figure 4A demonstrates that the main effect of an increase in $[Na^+]_i$ was a shrinking of
218 the tonic and bursting domains and an expansion of the resting domain due to upregulation of
219 the hyperpolarizing effect of increased $[Na^+]_i$ on the pump current.

220 **The evolution of the SLE mediated by $[K^+]_o$ and $[Na]_i$**

221 In the previous section, the influence of $[K^+]_o$ and $[Na]_i$ on network behavior was examined
222 without accounting for the time factor. Here, we present a fast-slow system analysis approach
223 that considers the time evolution of ionic concentrations, as shown in Figure 2. Hence, we
224 assessed the dependence of the evolution of an SLE on externally manipulated changes in $[K^+]_o$
225 and $[Na]_i$ with fixed concentrations of all other ions. As in Figure 4A, the chloride concentration
226 in the somatic and dendritic compartments of the PY cells was set to 7 mM. To schematically
227 describe the extracellular potassium concentration time course from preictal to postictal state (as
228 shown in Figure 2D), we identified four distinct stages (as shown in Figure 4B top panel): I) a
229 sharp increase in $[K^+]_{o,soma}$, II) elevated $[K^+]_{o,soma}$, a slow increase in $[K^+]_{o,dend}$, III) a slow
230 decrease in $[K^+]_{o,soma}$ and $[K^+]_{o,dend}$, IV) a decrease in $[K^+]_{o,soma}$ and $[K^+]_{o,dend}$ back to their resting
231 values. Variations in potassium concentrations were accompanied by changes in $[Na^+]_i$ (Figure

2E). In the preictal period and during the SLE tonic firing phase, $[Na^+]_i$ in the soma and dendrite was stable, while it increased during the burst firing phase and reached a plateau toward the end of the episode. In the postictal period, $[Na^+]_i$ in both compartments slowly returned to the initial value. The time course of $[Na^+]_i$ approximating intracellular somatic and dendritic sodium evolution is shown in Figure 4B (middle panel). The corresponding representative PY cell activity is shown in Figure 4B (bottom trace). To distinguish different SLE phases, the PY cell activity pattern was marked using a color-code, as in Figure 4A. As $[K^+]_o$ and $[Na^+]_i$ followed their predefined time course, PY cells exhibited transition from rest to tonic firing, progressed into bursting with a slowing-down pattern and eventually returned to the resting state. In the postictal period (after stage IV), the $[Na^+]_i$ remained elevated for more than 40 seconds (Figure 4B middle panel) giving rise to an enhanced hyperpolarizing Na^+/K^+-pump current that reduced the excitability of the network and contributed to postictal depression, as described in the last paragraph (Figure 7). To further observe the time evolution of the SLE in the $[K^+]_{o,soma}$, $[K^+]_{o,dend}$ parameter space, we superimposed potassium changes on the bifurcation diagrams in Figure 4A. The distinct stages of the potassium time course are marked by arrows. The crossing of a color border by an arrow corresponds to a transition between different firing regimes. The initial increase of somatic $[K^+]_o$ (stage I) led to a transition from the resting state to tonic firing (Figure 4A, first panel), while a subsequent increase of dendritic $[K^+]_o$ (stage II) led to a transition from tonic firing to bursting (Figure 4A, middle panel). A subsequent decrease in somatic and dendritic $[K^+]_o$ (stage III) led to the termination of the SLE, as the cell activity reentered the resting state region (Figure 4A, last panel). After termination of the SLE, $[K^+]_{o,soma}$ and $[K^+]_{o,dend}$ returned to their resting values (stage IV in Figure 4A, last panel).

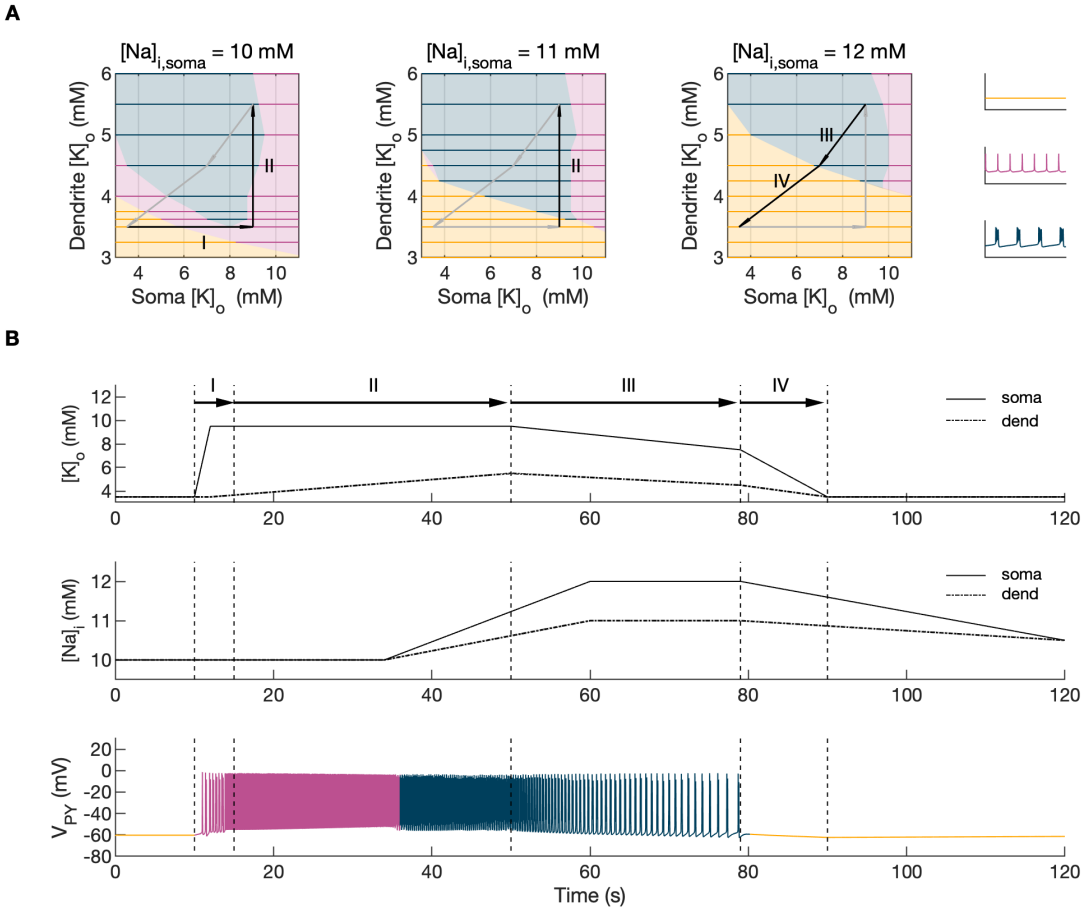

Figure 4. Analysis of the model. In the bifurcation analysis extracellular potassium and intracellular sodium concentrations in the PY and IN cells were control parameters. Concentrations of all other ions were fixed at their reference values (except chloride: $[Cl^-]_{i,soma}$, $[Cl^-]_{i,dend}$ equal to 7 mM), all ion accumulation mechanisms were blocked and background input was removed. **(A)** Bifurcation diagrams showing the dependence of the behavior of the model on $[K^+]_{o,dend}$ and $[K^+]_{o,soma}$ for varying values of $[Na^+]_{i,soma}$, $[Na^+]_{i,dend}$. The diagram colors correspond to types of activity shown on the right: rest (yellow), tonic firing (violet) and bursting (dark blue). An increase in $[Na^+]_i$ progressively decreased the domains of tonic firing and bursting and increased the resting domain indicating a general decrease in network excitability. The black and gray arrows correspond to the evolution of $[K^+]_{o,soma}$, $[K^+]_{o,dend}$ during different phases of the SLE, shown in part **B**. **(B)** A simulation of the model with $[K^+]_{o,soma}$, $[K^+]_{o,dend}$ and $[Na^+]_{i,soma}$, $[Na^+]_{i,dend}$ as the external control parameters, that illustrated the occurrence of transitions between different types of activity during the SLE. The top two panels show the time course of $[K^+]_{o,soma}$, $[K^+]_{o,dend}$ and $[Na^+]_{i,soma}$, $[Na^+]_{i,dend}$ and approximate their evolution during the SLE (Figure 2). The third panel shows the resulting PY cell behavior. The parameter

evolution is divided into four phases indicated by the arrows denoted as I–IV in part **A** and **B**. Phase I corresponds to a sharp increase in $[K^+]_{o,soma}$ which led to a transition from rest to tonic firing (marked as a black arrow 'I' in the first panel in **A**). Phase II corresponds to a slow increase in $[K^+]_{o,dend}$ which led to a transition from tonic firing to bursting (marked as a black arrow 'II' in the first and second panels in **A**). Phase III represents a period of increased $[Na^+]_{i,soma}$, $[Na^+]_{i,dend}$ and decreasing $[K^+]_{o,soma}$ and $[K^+]_{o,dend}$ which led to the termination of the SLE (represented by a black arrow 'III' with its tip in the yellow domain in the third panel in **A**). Phase IV corresponds to the postictal period with elevated $[Na^+]_i$ and a return of $[K^+]_{o,soma}$, $[K^+]_{o,dend}$ to their baseline values (marked as a black arrow 'IV' in the third panel in **A**).

The role of $[Cl^-]_i$

Chloride accumulation depends on Cl^- influx through chloride leak and GABAa receptor channels, but it is also affected by variations in potassium concentrations mediated via KCC2 cotransport. Hence, chloride and potassium could not be considered as independent control parameters in the fast-slow system analysis approach. Furthermore, visualization of the results with five control parameters ($[K^+]_{o,soma}$, $[K^+]_{o,dend}$, $[Na^+]_{i,soma}$, $[Na^+]_{i,dend}$ and $[Cl^-]_i$) is challenging. Therefore, to evaluate the role of chloride accumulation, we compared the reference model with the model in which chloride dynamics was excluded (Figure 5). When considering the role of chloride homeostasis mediated via KCC2, the direction of K–Cl cotransport depends on the E_{Cl} vs E_K or the ratio $[K^+]_i[Cl^-]_i/[K^+]_o[Cl^-]_o$ (Payne et al., 2003). If the ratio is greater than 1, KCC2 extrudes Cl^- and K^+. If E_K is greater than E_{Cl}, the KCC2 flow is reversed and Cl^- and K^+ ions are transported into the cell. When chloride accumulation was removed (Figure 5A), the reversal potentials of the Cl^- and GABAa currents (E_{Cl} and E_{GABAa}) were fixed (blue and light blue lines in Figure 5A, second panel). Under such conditions, the firing of the interneuron (Figure 5A, third panel) exerted a steady inhibitory influence on the PY cells. Additionally, it increased $[K^+]_o$ above fixed $[Cl^-]_i$ level (Figure 5A, fourth panel). As a result, E_K exceeded E_{Cl} and the KCC2 transported K^+ and Cl^- into the cells (Figure 5A, fifth panel) and reduced the external K^+ concentration. All these effects transiently increased the PY cells tonic firing but the bursting SLE phase was not manifested (Figure 5A, first and second panel). Conversely, activation of the IN in the reference model, with chloride dynamics intact, led to a typical SLE (Figure 5B, top panel). The $[Cl^-]_i$ accumulation was dominated by Cl^- influx through GABAa receptors and to lesser degree by KCC2 cotransport (Figure 5B, fifth and bottom panel). It led to enhanced excitability in two ways: i) by increasing the chloride reversal potential (blue line in Figure 5B,

second panel) toward the PY membrane potential, reducing the hyperpolarizing chloride leak current; ii) by increasing the GABAa reversal potential (Figure 5B, second panel, light blue) that approached the PY cell membrane potential, reducing the postsynaptic inhibitory current. These changes led to the stronger tonic firing of the PY cells, which contributed to enhanced $[K^+]_o$ accumulation (Figure 5B, third panel) leading to the transition into the SLE bursting phase.

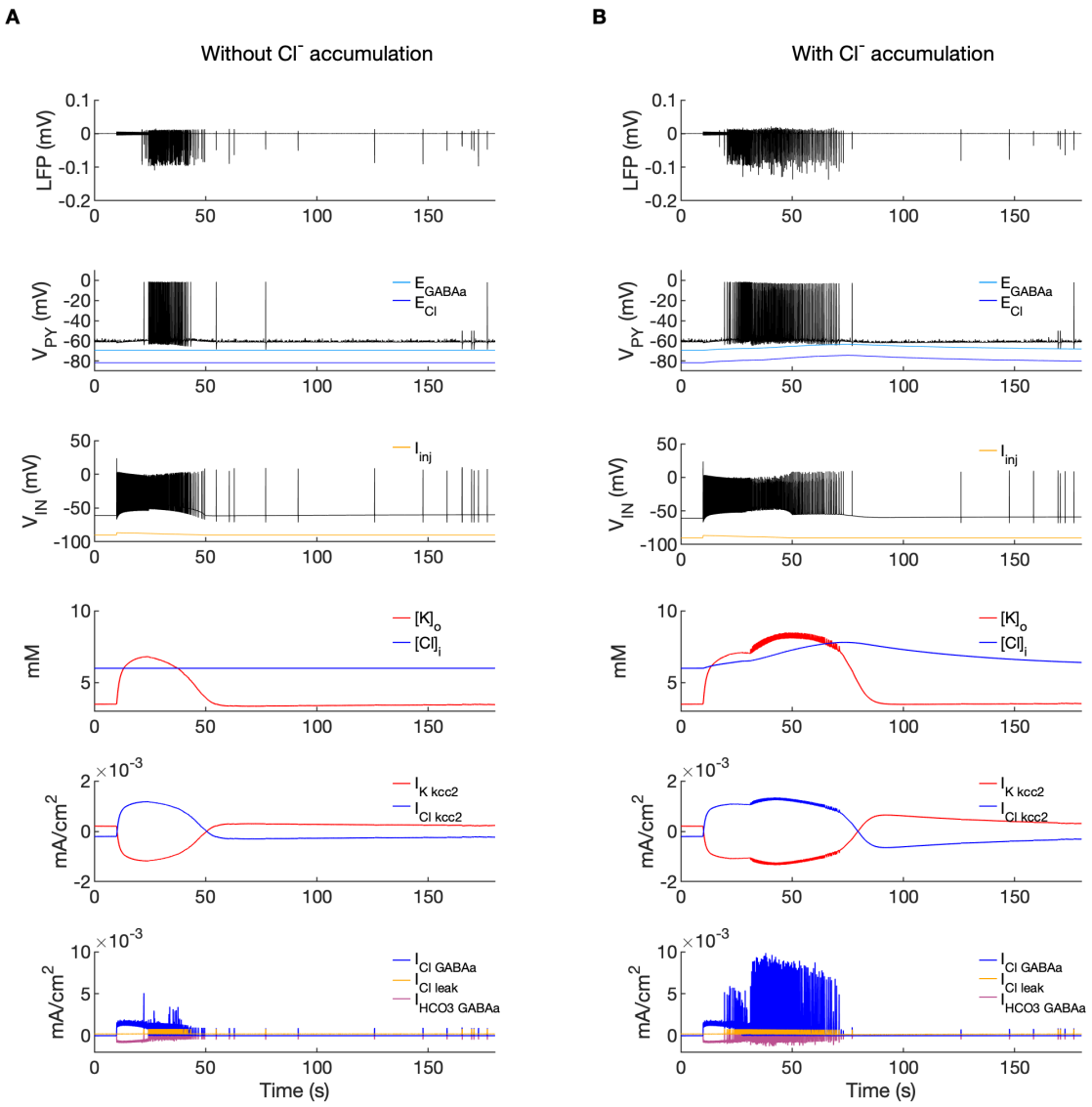

Figure 5. A comparison of the model without and with chloride accumulation. The six panels in each column show respectively (from top to bottom): the LFP signal, the PY cell membrane potential, the IN membrane potential, the extracellular potassium concentration and intracellular chloride concentration, the chloride and potassium KCC2 currents in the somatic compartments and the GABAa synaptic currents (Cl^- and HCO_3^-) together with the leak chloride

313 current. Additionally, the equilibrium potential of chloride and GABAa are shown in the second
314 panel from the top. **(A)** When the $[Cl^-]_i$ accumulation mechanism was blocked, the chloride
315 concentration was fixed at the reference value (fourth panel, blue). Without chloride
316 accumulation, the PY cell (second panel) fired tonic train of spikes due to transient rise in $[K^+]_o$
317 (fourth panel, red) mediated by the IN discharge triggered by the current injection (third panel,
318 yellow). Elevated $[K^+]_o$ and fixed $[Cl^-]_i$ promoted K^+ influx via KCC2 (fifth panel, red), thus
319 lowering $[K^+]_o$ and further preventing the generation of the full SLE. **(B)** With chloride
320 accumulation, the IN discharge led to an increase in E_{Cl} and E_{GABAa} (second panel, blue and light
321 blue) which reduced the hyperpolarizing $I_{Cl,leak}$ and I_{GABAa} currents and enhanced excitability.
322 The increase in firing rate of the PY cells led to prolonged $[K^+]_o$ accumulation (fourth panel, red)
323 leading to the full SLE.

324 **Model predictions**

325 The computer model generated predictions about features that were not explicitly implemented
326 but were consequences of the elementary neurobiological mechanisms used to create the model.
327 These phenomena are described below. The experimental confirmation of features predicted by
328 a model is an essential step in model validation.

329 *The evolution of the inter-burst interval duration*

330 It is well known that muscle jerking during the clonic phase of a tonic-clonic seizure slows down
331 before ceasing when seizure ends (Bromfield et al., 2006). Frequency slowing has also been
332 observed in video sequences (Kalitzin et al., 2016) and electrographic counterparts of a seizure
333 revealed by either EEG (Franaszczuk et al., 1998; Schiff et al., 2000) or EMG (Conradsen et al.,
334 2013). In the model, a gradual increase in the interval between ictal bursts (IBI) was visible
335 (Figure 2A and 3B). To observe the evolution of the IBI more precisely and identify the scaling
336 pattern, the background noise was removed from the simulation. The absence of excitatory
337 dendritic synaptic input was compensated with a steady depolarizing DC current of 1.85 pA
338 injected into the dendrites of all PY cells. Current intensity was adjusted to preserve the original
339 duration of the SLE as observed in the model with the background noise present. A simulated
340 SLE trace and the detected ictal bursts (short bars) are shown in Figure 6A (top panel). The
341 evolution of the IBI is shown below with either linear (Figure 6A, middle panel) or a logarithmic
342 (Figure 6A, bottom panel) y-axis. The IBI on the semi-log graph laid on a straight line suggesting
343 an exponential relationship. The evolution of the IBI during an SLE in a whole-brain *in vitro*

preparation (Figure 6B) and a human TLE seizure (Figure 6C) exhibited the same characteristics. Based on literature we considered four different scenarios of IBI evolution: linear, exponential, square root and logarithmic. The fits were evaluated by the root mean square error (RMSE). Exact RMSE values depended on the duration of the analyzed IBI sequence. In the model, RMSE values for logarithmic and exponential fits were often comparable. In the experimental data the exponential fit always had the lowest RMSE. Next, we used the fast-slow system analysis approach, as in Figure 4, to demonstrate how separate variations in $[K^+]_o$, $[Na^+]_i$ and $[Cl^-]_i$ affect IBI slowing towards the end of an SLE. Linear decrease in $[K^+]_o$ led to exponential IBI evolution, while linear increase in $[Na^+]_i$ or decrease in $[Cl^-]_i$ led to SLE termination with logarithmic scaling of IBI as determined by RMSE (Figure 6 – figure supplement 1). Note, that in this figure we simulated a decrease in $[Cl^-]_i$ unlike increasing trend in $[Cl^-]_i$ seen in Figure 2F. We observed that a linear increase in $[Cl^-]_i$ didn't lead to IBI slowing and SLE termination, when simulated for up to 20 min (not shown). These results suggest that in the model, slowing of inter-burst interval towards the end of an SLE is mediated by simultaneous changes in $[K^+]_o$ and $[Na^+]_i$.

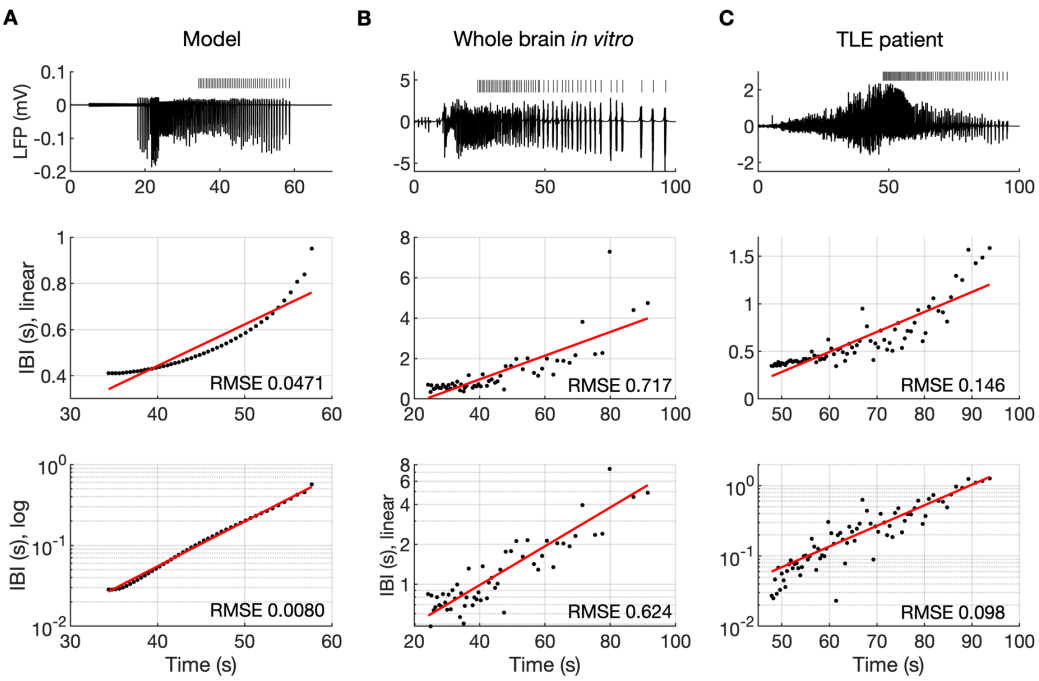

Figure 6. The evolution of inter-burst intervals (IBI) in the model and experimental data. (A) In the simulation, the background input was removed and compensated with a small depolarizing current injected into the PY cells to preserve the duration of the SLE. A decreasing rate of bursting is visible in the LPF signal and in the detected bursts marked above the trace (top panel). The evolution of the IBI is shown with the y-axis on a linear scale (middle panel) and a

364 log scale (bottom). On a linear y-axis plot, the data appear curved while on a semi-log plot they
365 lay on a straight line, suggesting exponential scaling of the IBI with time. The red line in each
366 plot represents the best fit for the detected IBI; linear function (middle panel) and exponential
367 function providing a linear relationship on a semi-log plot (bottom panel). The root mean square
368 error (RMSE) between the data points and fitted function is shown in each window. The
369 exponential function fit yielded a smaller RMSE compared to the linear, logarithmic or square
370 root fits (see Methods), providing quantitative confirmation that at the end of the simulated SLE,
371 the IBI duration increased exponentially with time. **(B)** The evolution of the IBI during the SLE
372 induced by application of bicuculline in the whole-brain *in vitro* preparation (Boido et al., 2014;
373 Gnatkovsky et al., 2008). **(C)** IBI evolution during a seizure recorded with intracerebral
374 electrodes positioned in the temporal lobe in a patient submitted to presurgical evaluation
375 (courtesy of Laura Tassi, Epilepsy Surgery Center, Niguarda Hospital, Milano, Italy). In **B** and
376 **C**, the detected IBI lay on a straight line on the semi-log plot and the exponential fit resulted in
377 a smaller RMSE compared to the linear, logarithmic or square root fits, validating the model
378 prediction of an exponential increase in the IBI at the end of a seizure. Only linear and
379 exponential fits are shown. The results for all considered fits are provided in Figure 6 – source
380 data 1.

381 *The postictal period*

382 An additional model prediction concerned the postictal period which is characterized by reduced
383 excitability and firing. As shown in Figure 2A–C, after the termination of an SLE there was an
384 approximate 90-second period during which firing was either absent or reduced with respect to
385 the interictal period. The exact duration of the postictal period was difficult to assess, as the gap
386 in firing after the SLE was dependent on background fluctuations. To directly investigate the
387 network excitability, we analyzed the responsiveness of the model to external periodic
388 stimulation (see Boido et al. (2014)). The background noise was removed and was compensated
389 with a steady depolarizing current, as in Figure 6. Stimulation was delivered by activating the
390 excitatory synapses every 5 seconds at each PY soma (arrows in Figure 7B). The amplitude of
391 the excitatory postsynaptic current was set at just above the threshold for triggering the spike in
392 the interictal period (before the timestamp at 60 seconds). The external stimulation triggered a
393 burst and two single spike responses after the SLE termination (Figure 7, vertical broken line)
394 and failed to trigger a suprathreshold response for approximately 90 seconds afterwards. In line
395 with the PY response pattern, no response to the simulated stimulation was observed in the LFP

signal during the postictal suppression period (Figure 7A). The high excitability immediately after termination of the SLE (timestamps between seconds 110 and 125) was correlated with elevated $[K^+]_o$ which was present shortly after the SLE (Figure 7C). The subsequent postictal reduction of excitability was associated with decay of $[K^+]_o$ and an increased hyperpolarizing Na^+/K^+-pump current in somatic and dendritic compartments. The pump current decayed with a slower time constant associated with a gradual clearance of $[Na^+]_i$ by the pump (Figure 7DE).

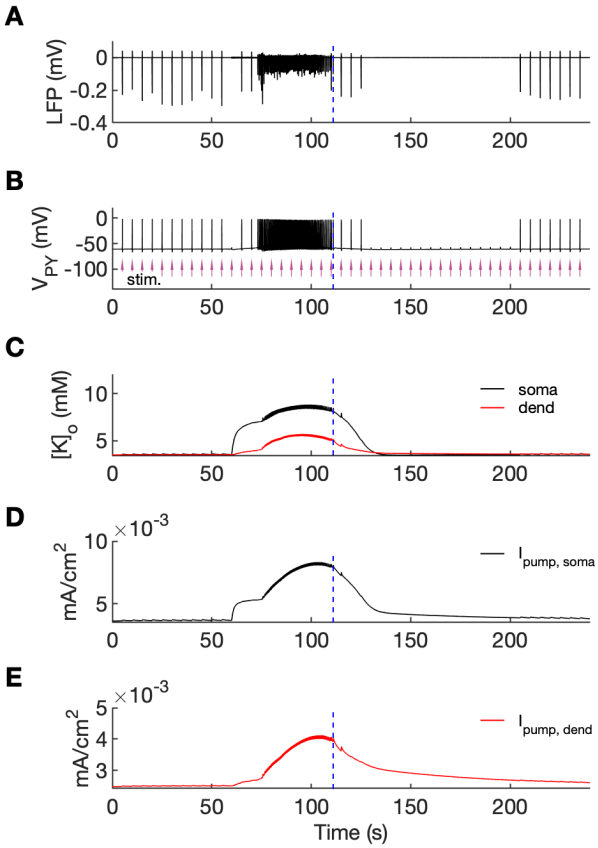

Figure 7. An analysis of network excitability in the postictal period. In this figure, the background input was removed from the simulation and compensated with a small depolarizing current injected into the PY cells, as in Figure 6. **(A)** The LFP signal. **(B)** The PY cell membrane potential with external periodic stimulation delivered every 5 seconds, marked by the arrows (violet, stim.). The amplitude of the stimulation was set at just above the threshold for triggering a spike in the interictal period. **(C)** The extracellular potassium in the somatic and dendritic compartments. **(D** and **E)** The net Na^+/K^+-pump current in the somatic and dendritic compartment, respectively. The vertical broken line (blue) in all panels marks the SLE offset time without periodic stimulation. Immediately after termination of the SLE, the network was still excitable due to increased $[K^+]_o$. Shortly afterward, the excitability decreased due to an

increased Na^+/K^+-pump current that outlasted the increase in $[K^+]_o$. Increased I_{pump} and decreased $[K^+]_o$ which occurred shortly after the termination of the SLE, led to a postictal period during which the network did not respond to external stimulation for approximately 90 seconds.

Discussion

The present study aimed to better define the mechanisms underlying focal seizures. The ictal pattern most frequently observed in human and experimental TLE, i.e., the LVF onset pattern, exhibits a stereotypical sequence of fast activity, irregular spiking and periodic bursting (as shown in Figure 3A, first panel) (Avoli et al., 2016; de Curtis & Avoli, 2016; Devinsky et al., 2018; Velascol et al., 2000). We successfully reproduced this pattern in the computer model by transiently increasing the firing of the IN. After this trigger, the simulated SLE phases evolved autonomously. Our study suggests that various seizure phases and transitions from one phase to another are mediated by feedback mechanisms between neuronal activities, ion concentration changes and ion homeostasis processes. The distinct mechanisms that shape the activities at various seizure stages are discussed below.

Seizure initiation

There is increasing evidence showing that seizures with LVF onset are initiated by discharges of fast-spiking GABAergic interneurons (de Curtis & Avoli, 2016; de Curtis & Gnatkovsky, 2009; Devinsky et al., 2018). Increased interneuron discharges and decreased PY activity around the time of seizure onset were first evidenced in *in vitro* and *in vivo* animal models (Gnatkovsky et al., 2008; Grasse et al., 2013; Lévesque et al., 2016; Lopantsev & Avoli, 1998; Miri et al., 2018; Toyoda et al., 2015; Ziburkus et al., 2006). A similar scenario was observed with single-unit recordings performed during intracerebral presurgical monitoring in neocortical and temporal lobe epilepsy patients (Elahian et al., 2018; Truccolo et al., 2011). Causal relationship between increased interneuron firing and ictogenesis may include intracellular chloride accumulation resulting in a shift in E_{GABAa} and/or the elevation of $[K^+]_o$, which leads to subsequent depolarization of PY cells and seizure development (Magloire, Mercier, et al., 2019). The hypothesis suggested by Jensen & Yaari (1997) that seizure initiation is related to an elevation in $[K^+]_o$ caused by a strong initial discharge has been tested in computational models with ion concentration changes. In these simulations, seizure-like activity has been induced by DC stimulation of the PY cells alone (Bazhenov et al., 2004; Buchin et al., 2016; Kager et al., 2002),

443 by a brief increase in $[K^+]_o$ (Fröhlich et al., 2006), by stimulation of the IN and PY cells (Ho &
444 Truccolo, 2016) or by varying the extracellular concentration of K^+ and O_2 (Wei, Ullah, & Schiff,
445 2014). However, as mentioned above, transitions to spontaneous seizures that begin with LFV
446 pattern were not associated with increased excitatory activity, but with increased firing of
447 inhibitory interneurons. Pyramidal cell – interneuron interplay during SLE was first investigated
448 in the computational model of Wei, Ullah, Ingram, et al. (2014) which mimicked 4-
449 aminopyridine (4-AP) and decreased magnesium *in vitro* conditions (Ziburkus et al. 2006). They
450 showed that when potassium diffusion rate around the IN was lower than around the PY cell, the
451 IN depolarized and increased its activity and eventually entered depolarization block giving way
452 to the strong firing of the PY cell during an SLE. The following *in silico* tests on seizure initiation
453 by selective involvement of fast-spiking interneurons were conducted by us (Gentiletti et al.,
454 2017) and others (González et al., 2018). We demonstrated that an increase in interneuron firing
455 triggered a transition to a self-sustained SLE during which both IN and PY cells were active
456 simultaneously. González et al. (2018) showed that interneuron stimulation by current pulses led
457 to the development of an SLE via a gradual increase in $[K^+]_o$ mediated the KCC2 cotransporter.
458 Activation of the KCC2 pump was $[Cl^-]_i$ dependent, while $[K^+]_o$ influenced cotransporter time
459 constant.

460 In the current study, an SLE was initiated by increased IN firing rate in response to
461 depolarizing current injection. We didn't attempt to demonstrate the mechanism leading to
462 increase in IN activity following bicuculline application in the isolated guinea pig brain, as the
463 mechanisms underlying this phenomenon are not fully understood. A decrease in GABAa
464 conductance by bicuculline likely affects interneuron-interneuron inhibition more than
465 interneuron-principal cell inhibition (Gnatkovsky et al., 2008). Accordingly, reciprocal release
466 of inhibition between the IN cells (i.e., disinhibition) may lead to preictal interneuronal spikes
467 contributing to increase in extracellular potassium. It would further depolarize interneuronal
468 network and initiate SLE (de Curtis & Avoli, 2016; Figure 4). In an alternative scenario,
469 increased excitability of interneurons could lead to a transition in a bistable IN network, from
470 asynchronous low firing mode to synchronous high firing rate mode due to small perturbation
471 (Rich et al., 2020). In order to fully investigate these effects using a model, one should consider
472 extended interneuronal network with mutual inhibitory interactions. In the current study we
473 focused on SLE initiation mediated by increased discharge of interneurons, without simulating
474 the underlying processes. It makes the model more general and corresponding to commonly
475 observed paradoxical increase in GABAergic cell firing at the LVF seizure onset. In our present

476 model, the IN was activated by a depolarizing, decreasing current ramp of 40 seconds. The IN
477 discharge initially led to the silencing of the PY cells, which was correlated with low amplitude
478 fast activity in the LFP signal. The sustained interneuron activity caused a gradual increase in
479 $[Cl^-]_i$ and $[K^+]_o$ in the PY cells. The increase in $[K^+]_o$ produced a positive shift in the K^+ reversal
480 potential which led to a reduction in the K^+ leak current and membrane depolarization. The
481 accumulation of $[Cl^-]_i$ increased the Cl^- reversal potential and decreased the driving force of the
482 Cl^- ions, which led to a reduction in GABAa IPSC and the Cl^- leak current. A depolarization in
483 the E_K, E_{Cl} and E_{GABAa}, and a weakening of the associated hyperpolarizing currents resulted in a
484 gradual depolarization of the PY cells and sustained firing, which was correlated with the tonic
485 SLE phase.

486 To address the role of potassium and chloride accumulation in seizure initiation, we
487 considered the elevation of $[K^+]_o$ and $[Cl^-]_i$ separately. As shown in Figure 5, a selective increase
488 in $[K^+]_o$ with a fixed concentration of Cl^- did not trigger full SLE. When $[Cl^-]_i$ was increased and
489 the concentration of K^+ remained fixed at the reference level the PY cells exhibited normal
490 background firing (not shown). This suggests that in our model a change in both $[K^+]_o$ and $[Cl^-$
491 $]_i$ act in synergy to mediate full SLE. These findings corroborate the results of a study by Alfonsa
492 et al. (2015) which demonstrated that optogenetic chloride loading of PY cells did not trigger
493 ictal events, while the addition of a subictal dose of 4-AP led to full ictal activity. Our results
494 don't contradict *in vitro* experimental observations that elevated $[K^+]_o$ alone is sufficient to
495 induce epileptiform activity (Jensen & Yaari, 1997; Traynelis & Dingledine, 1988). As shown
496 by a bifurcation diagram (Figure 4A and Appendix I – figure 1) an increase in $[K^+]_o$ may lead to
497 a transition from a silent state to tonic and burst firing.

498 Although in our model chloride accumulation increased E_{GABAa} and lowered synaptic
499 inhibition contributing to full-blown SLE, we didn't observe depolarizing GABA responses as
500 seen in some *in vitro* studies (Cossart et al., 2005; Miles et al., 2012; Ellender et al., 2014). It
501 should be kept in mind that depolarizing GABA responses were found mainly in immature
502 neurons, which have more depolarized Cl^- gradient (Cherubini et al., 1991). Another possible
503 explanation of the limited shift in E_{GABAa} in the model may be related to somatic localisation of
504 inhibitory input from the IN. Following the observation that activation of parvalbumin-positive
505 (PV) interneurons was implicated in spontaneous seizures (Toyoda et al., 2015) we simulated
506 soma-targeting, PV interneurons but not dendrite-targeting, somatostatin-expressing (SST)
507 interneurons. To see if a more pronounced shift in E_{GABAa} could be observed in SST interneuron

508 mediated dendritic responses we reduced the size of all model compartments to account for distal
509 dendrites. Under these conditions, strong activation of inhibitory interneuron as in Kaila et al.
510 (1997) led to biphasic, hyperpolarizing-depolarizing GABAa response shown in Appendix I –
511 figure 3. These results are in agreement with other studies suggesting that $[Cl^-]_i$ can change
512 rapidly and contribute to depolarizing GABAa responses especially in the structures with low
513 volume to GABAa receptor density ratio (Staley et al., 1995; Staley & Proctor, 1999).

514 The observation that the development of seizures may be related to an increase in $[K^+]_o$
515 beyond the physiological values suggests that the modulation of $[K^+]_o$ by the use of K^+ chelators
516 is a potential strategy for the control of seizures. In our previous work, we demonstrated that an
517 artificial potassium buffer, which mimicked the function of astrocytes by balancing neuronal K^+
518 release, could reduce neuronal excitability and prevent an SLE (Suffczynski et al., 2017).

519 **The mechanisms of $[K^+]_o$ accumulation**

520 A question arises: what causes $[K^+]_o$ accumulation? The buildup of Cl^- inside the PY neurons
521 during interneuron-induced GABA release results in the activation of the KCC2 cotransporter,
522 which extrudes Cl^- and K^+ into the extracellular space. This hypothesis is supported by *in vitro*
523 experiments which showed that activation of GABAa receptors led to an increase in $[K^+]_o$ and
524 cell depolarization, which were eliminated by the KCC2 inhibitor, furosemide (Viitanen et al.,
525 2010). The above-mentioned hypothesis is also consistent with the findings that the application
526 of the KCC2 blockers VU0240551 and bumetanide prevented SLEs during 4-AP application in
527 rat brain slices (Hamidi & Avoli, 2015). However, it is not clear whether the ictal activity is
528 consistently based on K^+ efflux through KCC2. In the pilocarpine model, the enhancement of
529 KCC2 in principal cortical neurons is associated with a reduction in seizure duration (Magloire,
530 Cornford, et al., 2019). Based on these results, the authors suggested that KCC2 activity does
531 not affect seizure initiation, but influences seizure maintenance during a prolonged period of Cl^-
532 accumulation. The antiepileptic role of enhanced KCC2 activity has also been suggested by
533 Moore et al. (2018), who showed that KCC2 potentiation delayed the onset of an SLE after 4-
534 AP application *in vitro* and reduced the severity of kainate-induced seizures *in vivo*. When
535 considering the role of KCC2 in $[K^+]_o$ and $[Cl^-]_i$ accumulation, it is necessary to note that the
536 direction and magnitude of KCC2 transport depend on the concentration gradients of Cl^- and K^+
537 (Kaila et al., 2014). Under normal conditions, when $[K^+]_o$ is sufficiently controlled by
538 homeostatic mechanisms, GABAergic activity leads to the extrusion of Cl^- and K^+ by KCC2.
539 However, an increase in $[K^+]_o$ may reverse the K^+–Cl^- cotransport, thus contributing to $[K^+]_o$

buffering rather than accumulation (Payne, 1997; Thompson & Gahwiler, 1989) The activation of IN in our model led to a rapid increase in $[K^+]_o$ in the narrow extracellular interstitial compartments, while intracellular Cl^- accumulation was more gradual (Figure 2). This generated an influx of K^+ and Cl^- via KCC2 (Figure 5B), which led to $[K^+]_o$ buffering and $[Cl^-]_i$ accumulation. The exclusion of KCC2 involvement in the increase in $[K^+]_o$ suggests that the primary mechanism of $[K^+]_o$ accumulation in our model was due to other processes, such as the outward K^+ current that repolarizes action potentials in activated IN and PY cells. This observation is consistent with *in vivo* experimental evidence that showed a significant local $[K^+]_o$ rise due to increased spiking activity following electrical stimulation of the cat cerebral cortex (Heinemann & Lux, 1975).

It is worth noting that in our model KCC2 resumes extruding Cl^- shortly after SLE termination (Figure 5B). Accordingly, $[Cl^-]_i$ build up is observed over the whole SLE. Intracellular chloride imaging during SLE induced *in vitro* by Mg^{2+}-free solution showed that $[Cl^-]_i$ started to decline before the end of SLE (Raimondo, 2013), while during SLE induced *in vivo* by 4-AP $[Cl^-]_i$ recovery begun instantly after SLE offset (Sato et al., 2017). These dissimilar observations might be related to distinct firing patterns of inhibitory and excitatory neurons in 4-AP and low Mg^{2+} seizure models (Codadu et al., 2019), which in turn could lead to different Cl^- and K^+ and accumulation patterns.

The tonic-to-bursting transition

Potassium ions released by interneuron discharges initially diffused to the somatic extracellular compartments of the PY cells and contributed to PY soma depolarization and tonic firing, as described above. The initial fast rise of $[K^+]_o$ in the somatic compartment and slower rise in dendritic segment (Figure 2D) was related to the localization of inhibitory neuron near the PY soma. Subsequently, K^+ diffusion from the somatic to dendritic compartments promoted regenerative dendritic spikes in PY cells. In the model, the dendritic conductance of voltage-gated K^+ currents associated with spiking was about 10% of the somatic conductance (Fransen et al., 2002) hence release of K^+ ions into the dendritic interstitial space was smaller than in the somatic compartment. On the other hand, radial diffusion and glial buffering processes had the same efficiency in both compartments maintaining lower dendritic $[K^+]_o$. This model prediction appears to agree with experimental data of simultaneous recordings of $[K^+]_o$ in somatic and dendritic layers during hippocampal seizures in anesthetized rats. During paroxysmal firing

571 induced by electrical stimulation, $[K^+]_o$ in dentate gyrus reached significantly higher levels in
572 cell body layers than in the layers containing dendrites (Somjen & Giacchino, 1985). High $[K^+]_o$
573 in the soma and moderately increased $[K^+]_o$ in dendrites favored burst firing (Figure 4A and
574 Appendix I – figure 1) through the reduction of repolarizing K^+ currents, the activation of a Na^+
575 persistent current, and a shift from spike after-hyperpolarization toward depolarizing after-
576 potentials. Prolonged depolarization led to the activation of slow M-type K^+ conductance
577 (Appendix I – figure 2), which hyperpolarized the PY cells after a series of fast spikes. The
578 bursting mechanism in our model originated from currents used in the original entorhinal cortex
579 cells model (Fransen et al., 2002) and was similar to the mechanism in CA1 neurons (Golomb
580 et al., 2006).

581 We note that in our model a transition from resting to tonic and then to bursting activity
582 in PY cells was not critically dependent on perisomatic inhibition and would be also observed if
583 we simulated dendrite-targeting, SST interneurons. As shown by the bifurcation diagram in
584 Figure 4A (first panel) an increase in either somatic or dendritic $[K^+]_o$ may lead to a transition
585 from rest to tonic spiking and then bursting. This observation is in agreement with the study
586 showing that optogenetic activation of either PV or SST inhibitory interneurons can trigger SLE
587 (Yekhlef et al., 2015).

588 **Seizure termination**

589 Various mechanisms underlying seizure termination have been suggested (Lado & Moshé, 2008;
590 Zubler et al., 2014), however, researchers have not yet reached a consensus regarding which one
591 plays a dominant role. In our model, the SLE terminated spontaneously. Following the fast-slow
592 analysis approach (Fröhlich et al., 2006) we created a simplified model in which $[K^+]_{o,soma,}$
593 $[K^+]_{o,dend}$ together with $[Na^+]_{i,\ soma}$ and $[Na^+]_{i,\ dend}$ were treated as control parameters. Hence, the
594 influence of neuronal activity on ionic variations was removed and the dependence of network
595 activity on K^+ and Na^+ concentrations was analyzed (Figure 4A). When the time course of the
596 concentration changes of these two ions were tuned to reproduce the decrease in $[K^+]_o$ and
597 maintained increased level of $[Na^+]_i$ observed in the late SLE phase, the ictal activity
598 spontaneously terminated (Figure 4B). This indicates that SLE cessation in the model can be
599 explained by two coincident factors, namely the decrease in $[K^+]_o$ during stable levels of
600 increased $[Na^+]_i$. An increase in $[Na^+]_i$ led to an increased hyperpolarizing Na^+/K^+-pump current,
601 which increased the firing threshold in the neurons. The increased pump activity also contributed

602 to a progressive decrease in $[K^+]_o$. Potassium repolarization currents increased after each burst
603 and eventually prevented the initiation of a new cycle of the oscillation. The idea that negative
604 feedback between $[Na^+]_i$ accumulation and neuronal firing is responsible for seizure termination
605 was first formulated by Jensen & Yaari (1997). Even though it has not been tested
606 experimentally, this hypothesis is consistent with the observation that the inhibition of Na^+/K^+-
607 pump activity occurring during hypoxia prolongs SLE discharges and shortens post-SLE period
608 in hippocampal slices with blocked synaptic transmission (Haas & Jefferys, 1984). It was also
609 observed that a decrease in Na^+ channel conductance via the antiepileptic drug phenytoin,
610 increased the seizure threshold but prolonged the afterdischarges and seizure durations in the rat
611 kindling model of epilepsy (Ebert et al., 1997). In the computational model developed by the
612 Bazhenov team (Krishnan et al., 2015; Krishnan & Bazhenov, 2011) and Chizhov et al. (2018),
613 a progressive increase in $[Na^+]_i$ and activation of the electrogenic Na^+/K^+-pump were identified
614 as the primary factor of SLE termination. The seizure termination mechanism in the above-
615 mentioned studies is similar to the mechanism observed in the present study, even though
616 different specifications of neuronal mechanisms, network characteristics and seizure
617 morphologies were used.

618 It should be also noted that activation of the Na^+/K^+-pump by $[Na^+]_i$ is not the only
619 proposed mechanism of seizure termination. An alternative mechanism, also linked to an
620 increase in $[Na^+]_i$, is dependent on the Na^+-activated K^+ channels (Igelström, 2013). Moreover,
621 many other mechanisms such as acidosis (Ziemann et al., 2008), the upregulation of inhibitory
622 neurons (Wen et al., 2015), glutamate depletion (Lado & Moshé, 2008), the depolarization block
623 of neurons mediated by K^+ release from astrocytes (Bragin et al., 1997), after-hyperpolarization
624 due to K^+ channels (Timofeev & Steriade, 2004), postburst depression (Boido et al., 2014),
625 increased synchrony (Schindler et al., 2007) and the release of adenosine (During & Spencer,
626 1992; Uva & de Curtis, 2020) have been suggested to play a role in seizure termination.

627 The abrupt termination of a seizure across the entire brain (Salami et al., 2022) requires
628 long-range communication which may involve thalamocortical interactions (Aracri et al., 2018;
629 Evangelista et al., 2015), travelling waves (Martinet et al., 2017; Proix et al., 2018) and ephaptic
630 interactions (Jefferys, 1995; Shivacharan et al., 2019). Multiple neuromodulatory, ionic, synaptic
631 and neuronal components likely cooperate to terminate a seizure. Further insight into these
632 mechanisms may be obtained by their selective blockage (Uva & de Curtis, 2020), the tracking

633 of EEG signal changes as seizure offset approaches (Boido et al., 2014; Saggio et al., 2020) and
634 from analysis of the duration of postictal suppression (Payne et al., 2018).

635 **Frequency Slowing**

636 The approach of seizure termination is often (but not always) accompanied by an increase in the
637 intervals between successive bursts that form the late seizure phase. Saggio et al. (2020) analyzed
638 frequency slowing in human focal onset seizures and estimated that approximately 40%
639 exhibited unequivocal discharge slowing down toward the end. Burst frequency slowing was
640 confirmed in a study on the entorhinal cortex of the isolated brain preparation during bicuculline-
641 and 4AP-induced SLE (Boido et al., 2014). Our model prediction of the exponential increase in
642 the IBI toward the SLE offset (Figure 6A) was confirmed with experimental data (Figure 6BC).
643 These findings are also consistent with those of Bauer et al. (2017), which demonstrated that
644 inter-burst intervals in focal epilepsy patients were predominantly described by the exponential
645 scaling law. Conversely, it has been suggested that depending on the bifurcation which leads to
646 seizure termination, the burst oscillation frequency can be constant or decrease according to the
647 logarithmic or square root relationship (Izhikevich, 2000; Jirsa et al., 2014). This theory has not
648 been confirmed by our model and experimental seizure data (Figure 6). On the other hand, when
649 specific ion types were varied linearly and led to linearly decreasing membrane current (not
650 shown), logarithmic increase in IBI was observed (Figure 6 – figure supplement 1BC). It shows
651 that when the assumption of slow linear membrane current dynamics was satisfied, the IBI
652 evolved according to the bifurcation theory. However, when various processes influenced
653 seizure termination and the current changed non linearly, the IBI slowing deviated from the
654 predicted scaling laws.

655 In our model, progressive decrease in neuronal excitability related to simultaneous
656 decrease in $[K^+]_o$ and increase in $[Na^+]_i$, was responsible for the IBI slowing towards an SLE
657 end. Alternative explanations for the increasing inter-burst intervals have been proposed. Bauer
658 et al. (2017) included a plasticity parameter that progressively decoupled spatially distributed
659 neural mass units based on the synchrony level. This mechanism accounted for seizure
660 termination, exponential IBI increase and the presence of a transient postictal state. In the model
661 of Liou et al. (2020) the IBI was constant during seizure expansion and only when the spatial
662 propagation of ictal discharge ceased, the seizure entered the pre-termination stage with a
663 slowing-down trend. An increase in the IBI in this phase was related to the recovery of inhibition

and restoration of the Cl^- concentration gradient. These studies indicate that spatial properties related to seizure propagation and synchrony are other factors that may affect the evolution of the IBI.

The postictal period

Seizures are followed by the suppression of physiological rhythms known as postictal EEG suppression (PES) that lasts for seconds or minutes (Pottkämper et al., 2020). Using the stimulation protocol, we investigated the duration of PES in the model. Our results showed that shortly after termination of the SLE, burst responses were still triggered, however, after few seconds, the excitability decreased and remained reduced for approximately 90 seconds (Figure 7B). The PES duration in our model is consistent with a typical 'seconds to minutes' timescale although available estimates depend on the PES duration assessment method. In single-unit recordings in epileptic patients with neocortical seizures neuronal spiking was fully suppressed for 5 to 30 seconds after seizure termination (Truccolo et al., 2011). Average duration of postictal suppression based on EEG features in focal seizure patients was estimated at 17 s (Grigorovsky et al., 2020; Table 1), 120 s (D. E. Payne et al., 2018; Table 1) and around 50-100 s (Bauer et al., 2017; Figure 5). Our *in silico*-derived prediction that postictal 'silence' depends on the increased rate of hyperpolarizing Na^+/K^+-pump has been previously suggested (Fisher & Schachter, 2000) and simulated (Krishnan et al., 2015; Krishnan & Bazhenov, 2011). In these models, postictal state was generated via both, reduced $[K^+]_o$ to below baseline level and increased $[Na^+]_i$ after termination of an SLE. $[K^+]_o$ decrease below baseline resulted in a negative shift in E_K and membrane hyperpolarization, while elevated $[Na^+]_i$ increased Na^+/K^+-pump hyperpolarizing current. A below-reference value of $[K^+]_o$ was indeed observed after seizure termination (Heinemann et al., 1977). On the other hand, in other studies, $[K^+]_o$ decayed to baseline level after an SLE offset (Fisher et al., 1976; Futamachi et al., 1974) and couldn't contribute to the postictal state. Also in our model $[K^+]_o$ undershoot was not observed (Figure 7C), suggesting that the main cause of postictal reduction in excitability was hyperpolarizing effect of the Na^+/K^+-pump current, which remained elevated above baseline for about 100 s after SLE termination (Figure 7DE). The findings generated by our computational model suggest that ion homeostatic processes activated and sustained by the excessive seizure discharges provide a negative feedback mechanism, eventually leading to the cessation of the seizure itself and to the restoration of the normal state after a transitional period of postictal silence.

Methods

Geometry

The cell morphology was based on entorhinal cortex PY cells and an interneuron model (Fransen et al., 2002), further reduced to equivalent cylinder models. The PY consisted of two compartments: a soma with a length of 20 µm and a diameter of 15 µm, and a dendrite with a length of 450 µm and a diameter of 6.88 µm. The interneuron only had a somatic compartment with a length of 20 µm and a diameter of 15 µm. Each compartment was surrounded by its own extracellular space (ECS). The extracellular compartments were embedded in a common bathing medium which represented the surrounding neural tissue and vasculature. The size of the ECS was estimated by the extracellular volume fraction, α defined as the ratio volume of extracellular space/volume of tissue. We used α = 0.131 which corresponded to the CA1 *st. pyramidale* and a K^+ concentration of 3.5 mM (McBain et al., 1990).

Biophysics

The active membrane currents in the PY were the fast Na^+ and K^+ currents (I_{Na} and I_{Kdr}, respectively) in both compartments and were responsible for action potential generation; a persistent Na^+ current, I_{NaP} in the soma; a high-threshold Ca^{2+} current, I_{CaL} in both compartments; a calcium-dependent after-hyperpolarization K^+ current, I_{KAHP} in both compartments; a fast calcium- and voltage-dependent K^+ current, I_{KC} in both compartments; and a noninactivating muscarinic K^+ current, I_{KM} in the soma. The IN included only the I_{Na} and I_{Kdr} currents responsible for spike generation. All the equations for the active currents were initially based on those described by Fransen et al. (2002), however, an additional modification of the parameters described below was required to account for ionic regulation mechanisms. Simulations were performed using the NEURON simulator with a fixed integration step of 0.05 ms.

Passive properties

The reversal potentials were obtained via the Nernst equation:

$$E_X = 2.3\frac{RT}{zF}\log\left(\frac{[X]_o}{[X]_i}\right)$$

where $[X]_i$ and $[X]_o$ are intra- and extracellular concentrations, respectively, of the ions. X = {Na^+, K^+, Ca^{2+}, Cl^-, HCO_3^-}, F is the Faraday constant, R is the gas constant, z is the valence of

the ions and T = 273,16 + 32 is the absolute temperature (Gnatkovsky et al., 2008). A leak current, I_{leak}, was present in all compartments of both cells and was a sum of the leak currents of Na^+, K^+ and Cl^-, modelled as:

$$I_{i,leak} = g_{i,leak}(V - E_i)$$

where $g_{i,leak}$ is the leak current conductance of the ion of interest i = {Na^+, K^+, Cl^-}. The resting membrane potential was -61 mV in the pyramidal cell and in the interneuron. The specific axial resistance in both cells was set to R_a = 100 Ohm*cm and the specific membrane capacitance was set to C_m = 1μF/cm^2, as in Fransen et al. (2002). Based on the R_a and PY cell geometry, the somato-dendritic coupling conductance, g_c, was calculated as 1.5 mS.

Active currents

The original equations used time constant units in seconds (s) and voltage units in volts (V), with 0 V corresponding to the resting membrane potential. All equations were modified to account for the millivolt (mV) and millisecond (ms) units used in our model and the voltage was shifted by -60 mV to correspond to the membrane potential relative to the extracellular space, which was assumed to be 0 mV. Additional modifications of the parameters were required to account for the ionic regulation mechanisms that were not present in the original model. I_{NaP}: the activation gate exponent was 2 and the inactivation gate time constant, τ_h, was estimated by fitting the activation function form described by Fransen et al. (2002) to the experimental data (Magistretti & Alonso, 1999). I_{Kdr}: the steady-state activation function, n_{inf}, and the activation gate time constant, τ_n, were estimated by empirical fit to the experimental data (Sah et al., 1988). To increase the firing threshold, the activation curve was shifted toward positive potentials by 18 mV in the soma and 10 mV in the dendrites. The model generated spontaneous fast spiking otherwise. I_{KAHP}, I_{KC}: these Ca^{2+}-dependent currents were modelled according to the model described by Traub et al. (2003) and were implemented in ModelDB (https://senselab.med.yale.edu/ModelDB/), accession number 20756. Due to the arbitrary units for Ca^{2+} concentration in Traub's model, we modified the current formula to correspond to mM units and resting level of $[Ca^{2+}]_i$ used in our model. In pyramidal cells, the soma and dendrite membrane potentials, V_s and V_d, respectively, were governed by the following Hodgkin-Huxley equations:

$$C\frac{dV_s}{dt} = -I_{Na,soma} - I_{NaP} - I_{Kdr,soma} - I_{CaL} - I_{KAHP} - I_{KC} - I_{KM}$$
$$- I_{leak} - I_{NaKpump} - I_{Capump} - g_c(V_s - V_d) - I_{syn}$$

$$C\frac{dV_d}{dt} = -I_{Na,dend} - I_{Kdr,dend} - I_{CaL} - I_{KAHP} - I_{KC} - I_{NaKpump} - I_{CaPump} - g_c(V_d - V_s) - I_{syn}$$

Transient sodium current

$$I_{Na,soma} = g_{Na,PYsoma} m^3 h(V - E_{Na})$$

$$I_{Na,dend} = g_{Na,PYdend} m^2 h(V - E_{Na})$$

Persistent sodium current:

$$I_{NaP} = g_{NaP} m^2 h(V - E_{Na})$$

Delayed rectifier:

$$I_{Kdr,soma} = g_{Kdr,PYsoma} n^4 (V - E_K)$$

$$I_{Kdr,dend} = g_{Kdr,PYdend} n^2 (V - E_K)$$

High-threshold Ca^{2+} current:

$$I_{CaL} = g_{CaL} m^2 (V - E_{Ca})$$

Ca^{2+}-dependent K^+ (afterhyperpolarization) current:

$$I_{KAHP} = g_{KAHP} m(V - E_K)$$

Fast Ca^{2+}- and voltage-dependent K^+ current

$$I_{KC} = g_{KC} \min([Ca^{2+}]_i/250,1)\, m(V - E_K)$$

Muscarinic current:

$$I_{KM} = g_{KM} m(V - E_K)$$

Equations of gating variables are given in Table 1. Conductance values are given in Table 2.

Table 1. Gating variables of the ionic currents in pyramidal cell model

Current	Kinetics/time constant (ms)	
$I_{Na,soma}$	$\alpha_m = \frac{0.8(-V-39.8)}{\exp\left(\frac{-V-39.8}{4}\right)-1}$	$\beta_m = \frac{0.7(V+14.8)}{\exp\left(\frac{V+14.8}{5}\right)-1}$
	$\alpha_h = 0.32\exp\left(\frac{-V-15}{18}\right)$	$\beta_h = \frac{10}{\exp\left(\frac{-V-15}{5}\right)+1}$
$I_{Na,dendrite}$	$\alpha_m = \frac{0.32(-V-48.9)}{\exp\left(\frac{-V-48.9}{4}\right)-1}$	$\beta_m = \frac{0.28(V+21.9)}{\exp\left(\frac{V+21.9}{5}\right)-1}$
	$\alpha_h = 0.128\exp\left(\frac{-V-44}{18}\right)$	$\beta_h = \frac{4}{\exp\left(\frac{-V-21}{5}\right)}$

I_{NaP}	$m_\infty = \frac{1}{1+\exp\left(\frac{-48.7-V}{4.4}\right)}$	$\tau_m = \frac{1}{\frac{0.091(V+38)}{1-\exp\left(\frac{-V-38}{5}\right)} - \frac{0.062(V+38)}{1-\exp\left(\frac{V+38}{5}\right)}}$
	$h_\infty = \frac{1}{1+\exp\left(\frac{48.8+V}{9.98}\right)}$	if $V_m \leq -60$: $\tau_m = 3700 + \frac{2000}{\frac{0.091(V+60)}{1-\exp\left(\frac{-V-60}{5}\right)} - \frac{0.062(V+60)}{1-\exp\left(\frac{V+60}{5}\right)}}$ if $V_m > -60$: $\tau_m = 1200 + \frac{8000}{\frac{0.091(V+74)}{1-\exp\left(\frac{-V-74}{5}\right)} - \frac{0.062(V+74)}{1-\exp\left(\frac{V+74}{5}\right)}}$
$I_{Kdr,soma}$	$n_\infty = \frac{1}{1+\exp\left(\frac{-20.8-V}{13.6}\right)}$	$\tau_m = \frac{1.6\left(C+\exp\left(\frac{V}{5}\right)\right)}{D\exp\left(-\frac{V}{40}\right)\left(C+\exp\left(\frac{V}{5}\right)\right)+0.016\exp\left(\frac{V}{5}\right)(64.9+V)}$ $C = -0.00000230599;\ D = 0.0338338$
$I_{Kdr,dend}$	$n_\infty = \frac{1}{1+\exp\left(\frac{-11.8-V}{13.6}\right)}$	$\tau_m = \frac{1.6\left(C+exp\left(\frac{V}{5}\right)\right)}{Dexp\left(-\frac{V}{40}\right)\left(C+exp\left(\frac{V}{5}\right)\right)+0.016\,exp\left(\frac{V}{5}\right)(64.9+V)}$ $C = -0.00000230599;\ D = 0.0338338$
I_{CaL}	$\alpha_m = \frac{1.6}{1+exp(-0.072(V-5))}$	$\beta_m = \frac{0.02(V+8.9)}{exp\left(\frac{V+8.9}{5}\right)-1}$
I_{KAHP}	$\alpha_m = 2000([Ca]_i - [Ca]_{i,rest})$	$\beta_m = 0.01$
I_{KC}, if $V_m \leq -10$	$\alpha_m = \frac{exp\left(\frac{V+50}{11} - \frac{V+53.5}{27}\right)}{18.975}$	$\beta_m = 2exp\left(-\frac{V+53.5}{27}\right) - \alpha_m$
I_{KC}, if $V_m > -10$	$\alpha_m = 2exp\left(-\frac{V+53.5}{27}\right)$	$\beta_m = 0$
I_{KM}	$m_\infty = \frac{1}{1+exp\left(-\frac{V+35}{5}\right)}$	$\tau_m = \frac{1000}{3.3\left[exp\left(\frac{V+35}{40}\right)\right]+\left[exp\left(-\frac{V+35}{20}\right)\right]}$

Membrane potential of the interneuron was governed by the following Hodgkin-Huxley equations:

$$C\frac{dV}{dt} = -I_{Na} - I_{Kdr} - I_{leak} - I_{NaKpump} - I_{syn} - I_{stim}$$

Current equations, kinetics and time constants of these currents were the same as in pyramidal cell soma. To prevent depolarization block of the IN during current stimulation, activation curve of I_{Na} was shifted 3 mV towards more negative potential values, while activation curve of I_{Kdr} was shifted 19 mV towards more negative potential values.

Table2. Conductances used in the model

Current conductance	Description	Values (S/cm^2)
$g_{Na,leak,PYsoma}$	$I_{Na,leak}$ conductance in PY soma	1.5*10^{-5}
$g_{Na,leak,PYdend}$	$I_{Na,leak}$ conductance in PY dendrite	1.1*10^{-5}
$g_{K,leak,PY}$	$I_{K,leak}$ conductance in PY soma and dendrite	3*10^{-5}
$g_{Cl,leak,PY}$	$I_{Cl,leak}$ conductance in PY soma and dendrite	1*10^{-5}
$g_{Na,PYsoma}$	I_{Na} conductance in PY soma	0.014
$g_{Na,PYdend}$	I_{Na} conductance in PY dendrite	0.0014
$g_{Kdr,PYsoma}$	I_{Kdr} conductance in PY soma	0.032
$g_{Kdr,PYdend}$	I_{Kdr} conductance in PY dendrite	0.0032
g_{NaP}	I_{NaP} conductance in PY soma	60*10^{-5}
g_{CaL}	I_{CaL} conductance in PY soma and dendrite	15*10^{-5}
g_{KAHP}	I_{KAHP} conductance in PY soma and dendrite	5*10^{-5}
g_{KC}	I_{KC} conductance in PY soma and dendrite	0.196*1e3
g_{KM}	I_{KM} conductance in PY soma	0.006
$g_{Na,leak,IN}$	$I_{Na,leak}$ conductance in IN	2.9*10^{-5}
$g_{K,leak,IN}$	$I_{K,leak}$ conductance in IN	6*10^{-5}
$g_{Cl,leak,IN}$	$I_{Cl,leak}$ conductance in IN	1*10^{-5}
$g_{Na,IN}$	I_{Na} conductance in IN	0.013
$g_{Kdr,IN}$	I_{Kdr} conductance in IN	0.027

Ionic dynamics

The model included six types of ions (K^+, Na^+, Cl^-, Ca^{2+}, A^- and HCO_3^-) with variable intra- and extracellular concentrations, except for HCO_3^-, which equilibrium is rapidly attained (Theparambil et al., 2020). The evolution of the ion concentrations was based on the following equations:

$$\frac{d[K^+]_i}{dt} = J_K^i + J_{K,longitudinal}^i + J_{K,KCC2}^i + J_{K,Pump}^i + J_{K,vol}^i$$

$$\frac{d[K^+]_o}{dt} = J_K^o + J_{K,radial} + J_{K,longitudinal}^o + J_{K,bath} + J_{K,KCC2}^o + J_{K,Pump}^o + J_{glia} + J_{K,vol}^o$$

$$\frac{d[Na^+]_i}{dt} = J_{Na}^i + J_{Na,longitudinal}^i + J_{Na,Pump}^i + J_{Na,vol}^i$$

$$\frac{d[Na^+]_o}{dt} = J_{Na}^o + J_{Na,radial} + J_{Na,longitudinal}^o + J_{Na,bath} + J_{Na,Pump}^o + J_{Na,vol}^o$$

$$\frac{d[Cl^-]_i}{dt} = J_{Cl}^i + J_{Cl,GABAa}^i + J_{Cl,longitudinal}^i + J_{Cl,KCC2}^i + J_{Cl,vol}^i$$

$$\frac{d[Cl^-]_o}{dt} = J_{Cl}^o + J_{Cl,GABAa}^o + J_{Cl,longitudinal}^o + J_{Cl,bath} + J_{Cl,KCC2}^o + J_{Cl,vol}^o$$

$$\frac{d[Ca^{2+}]_{i,tot}}{dt} = J_{Ca}^i + J_{Ca,longitudinal}^i + J_{CaPump}^i + J_{Ca,vol}^i$$

$$\frac{d[Ca^+]_o}{dt} = J_{Ca}^o + J_{Ca,longitudinal}^o + J_{CaPump}^o + J_{Ca,vol}^o$$

$$\frac{d[A^-]_i}{dt} = J_{A,vol}^i$$

where $[Ca^{2+}]_{i,tot}$ is the total intracellular calcium concentration (see calcium buffer below). All fluxes (mM/ms) are specified below.

Membrane currents

The contribution of transmembrane currents to variations in intra- and extracellular ion concentrations was obtained via the following equations:

$$J_X^i = -\frac{\sum I_X S}{zFV_i}$$

$$J_X^o = \frac{\sum I_X S}{zFV_o}$$

where the sum of I_X is a net membrane current carrying ion X, S is the surface area of the compartment, z is the valence of the ions, F is the Faraday constant and V_i and V_o are the volumes of the intra- and extracellular compartments.

Longitudinal diffusion.

Longitudinal diffusion of K^+, Na^+, Ca^{2+} and Cl^- was implemented between the somatic and dendritic compartments in the intracellular and extracellular space of the same cell. It was described by Fick's first law:

$$J_{X,longitudinal}^{io} = D_x \frac{([X]_{io,a} - [X]_{io})S}{LV_{io}}$$

where D_x is the diffusion coefficient for the ion X, $[X]_{io}$ is the ion concentration in a given intra- or extracellular compartment, $[X]_{oi,a}$ is the ion concentration in the adjacent compartment, S is the cross-sectional area between the compartments, V_{io} is the compartment volume, L is the distance between the centers of the compartments. The diffusion coefficients were (in um^2/ms): $D_{Na} = 1.33$, $D_K = 1.96$, $D_{Ca} = 0.6$, $D_{Cl} = 2.03$ (as in Somjen et al., 2008).

Radial diffusion.

Na^+ and K^+ ions diffused radially between adjacent extracellular compartments modeled as concentric shells around the neurons. The radial exchange of ions between adjacent shells was described by Fick's first law:

$$J_{X,radial} = D_x \frac{\sum([X]_{o,a} - [X]_o)S}{drV}$$

where $[X]_o$ is the ion concentration in a given shell and the sum goes over all adjacent shells having concentrations $[X]_{o,a}$, V is a given shell volume, dr is the distance between the centers of the shells and S is the surface contact area between the shells calculated at 16% of the total outer shell surface. The electrostatic drift of ions was neglected as the ion movement due to the electrical potential gradient in the extracellular space was small compared to the diffusion.

Diffusion to/from the bath

Radial diffusion of K^+, Na^+ and Cl^- between the ECS and the bath was described by Fick's first law:

$$J_{X,bath} = \frac{1}{s} D_x \frac{([X]_{bath} - [X]_o)S}{drV}$$

where D_x is the diffusion coefficient for the ion X, s is the scaling constant, S is the outer surface of the shell, $[X]_{bath}$ is the bath concentration of the ion X, $[X]_o$ is the ion concentration in a given shell, V is the shell volume, dr is the distance between the extracellular space and the bath (assumed to be half of the shell thickness). Flux J_{bath} represents various processes such as diffusion to more distant areas of the brain and cerebrospinal fluid, active transport of potassium into capillaries and potassium spatial buffering by astrocytes. The effective time constant of these joint processes is likely to be much slower than that of radial and longitudinal diffusion and is described by the scaling constant $s = 4.4*10^4$.

The Na^+/K^+ pump

The Na^+/K^+ pump was modelled as the sodium and potassium transmembrane currents (Kager et al., 2000):

$$I_{Na,Pump} = 3I_{max}flux([Na^+]_i, [K^+]_o)$$

$$I_{K,Pump} = -2I_{max}flux([Na^+]_i, [K^+]_o)$$

$$flux([Na^+]_i, [K^+]_o) = \left(1 + \frac{Km_K}{[K^+]_o}\right)^{-2} \left(1 + \frac{Km_{Na}}{[Na^+]_i}\right)^{-3}$$

with $Km_K = 2$ mM and $Km_{Na} = 10$ mM. I_{max} values were computed for each cell and compartment to balance Na^+ and K^+ membrane currents at rest and were as follows (in mA/cm^2): 0.014 (PY soma), 0.009 (PY dendrite), 0.025 (IN).

KCC2 cotransport

The KCC2 cotransporter currents were modelled according to Wei et al. (2014):

$$I_{K,KCC2} = U_{KCC2} \log\left(\frac{[K^+]_i[Cl^-]_i}{[K^+]_o[Cl^-]_o}\right)$$

$$I_{Cl,KCC2} = -I_{K,KCC2}$$

with cotransporter strength adjusted to balance chloride leak current at rest, U_{KCC2} = 0.002 mA/cm^2.

Glial uptake

Potassium uptake by the glia was modelled as a set of differential equations (Kager et al., 2000):

$$J_{glia} = -k_2[K^+]_o[B] + k_1[KB]$$

$$\frac{d[B]}{dt} = -k_2[K^+]_o[B] + k_1[KB]$$

$$\frac{d[KB]}{dt} = k_2[K^+]_o[B] - k_1[KB]$$

where *[B]* is the free buffer, *[KB]* is the bound buffer (= $[B]_{max}$–*[B]*), B_{max} = 1100 mM. k_1 = 0.0008 ms^{-1} and $k_2 = \frac{k_1}{1+\exp\left(\frac{[K]_o-16}{-1.25}\right)}$ are backward and forward rate constants, respectively.

The calcium pump and buffer

The calcium pump and buffer which altered the intracellular Ca^{2+} were modelled according to the model implementation of Somjen et al. (2008) in ModelDB, accession number 113446. The calcium pump which extruded Ca^{2+} from the cells was modelled as a Ca^{2+} transmembrane current:

$$I_{CaPump} = \frac{I_{max}}{1 + \frac{K_{pump}}{[Ca^{2+}]_i}}$$

with I_{max} = 2.55 mA/cm^2 and K_{pump} = 0.0069 mM. Intracellular Ca^{2+} was buffered by first-order chemical Ca^{2+} buffer with a total concentration of $[B]_i$ and an equilibrium constant of K_d. Calcium buffering was fast and under the assumption of equilibrium conditions, the relationship between the total and free intracellular calcium concentrations, $[Ca^{2+}]_{i,tot}$ and $[Ca^{2+}]_i$, was given by (Borgdorff, 2002, pg. 27):

$$[Ca^{2+}]_{i,tot} = [Ca^{2+}]_i \frac{[B]_i + K_d + [Ca^{2+}]_i}{K_d + [Ca^{2+}]_i}$$

where $[B]_i$ = 1.562 mM*(V_i^0/V_i), V_i is the intracellular compartment volume, V_i^0 is the intracellular compartment volume at rest and K_d = 0.008 mM.

Volume changes

Volume changes were modelled according to Somjen et al. (2008). The rates of intra- and extracellular volume changes were proportional to the difference in osmotic pressure between the intra- and extracellular compartments and fulfilled the conservation of total volume.

$$\frac{dV_i}{dt} = \Delta$$

$$\frac{dV_o}{dt} = -\Delta$$

where

$$\Delta = \frac{c(\pi_i - \pi_o)}{\tau}$$

$$\pi_i = [Na^+]_i + [K^+]_i + [Cl^-]_i + [Ca^{2+}]_i + [HCO_3^-]_i + [A^-]_i$$

$$\pi_o = [Na^+]_o + [K^+]_o + [Cl^-]_o + [Ca^{2+}]_o + [HCO_3^-]_o + [A^-]_o$$

V_i and V_o are the volumes of the intra- and extracellular compartments and τ = 250 ms. The constant c is introduced for unit conversion and is equal to 1 um^3/mM, hence units of Δ are um^3/ms. The extracellular volume was initially 13.1% of the cellular volume and was allowed to shrink maximally down to 4%. Volume changes affected concentrations but not the total mass of each ion within a compartment. The conservation of mass required additional fluxes:

Intracellular

$$J^i_{X,vol} = -\frac{\Delta}{V_i}[X]_i$$

Extracellular

$$J^{o}_{X,vol} = \frac{\Delta}{V_o}[X]_o$$

Extracellular space (ES) volume shrinks maximally by about 27%, comparable to average reduction of 30% during self-sustained epileptiform discharges (Dietzel et al., 1980). Intracellular space (IS) volume expands about 4%, being a consequence of constant total volume (ES+IS = const). Volume changes and resulting shifts in representative ion concentrations are shown in Appendix I – figure 4. We note that volume changes in our model didn't have big impact on the observed model dynamics. Shifts in ionic gradients contributed by slow volume changes were efficiently compensated by other homeostatic mechanisms, which acted on a faster time scale. In the real tissue astrocyte swelling may be significant and may reduce flow of ions and oxygen (affecting Na^+/K^+-pump activity) contributing to seizures and spreading depression (Hübel & Ullah, 2016). In our model glial cell swelling was not included and its effects on diffusion and the Na^+/K^+-pump were not simulated which is one of the model limitations.

Initial ion concentrations

The initial concentrations were based on existing literature: $[Na^+]_i$, $[Ca^{2+}]_i$, $[Na^+]_o$, $[K^+]_o$, $[Ca^{2+}]_o$ and $[A^-]_o$ (Somjen et al., 2008); $[Cl^-]_i$, $[HCO_3^-]_i$, $[HCO_3^-]_o$ (Doyon et al., 2011); $[K^+]_i$ $[Cl^-]_o$ (Payne et al., 2003). In setting chloride and potassium concentrations we additionally aimed to fulfill $E_K < E_{Cl}$ and $E_{GABAa} \sim -70$ mV (Andersen et al., 1980). The $[A^-]_i$ concentration was set to fulfill osmotic equilibrium condition. Hence, the initial concentrations were as follows (in mM): $[Na^+]_i = 10$, $[Na^+]_o = 140$, $[K^+]_i = 87$, $[K^+]_o = 3.5$, $[Cl^-]_o = 135$, $[Cl^-]_i = 6$, $[Ca^{2+}]_i = 5e\text{-}5$, $[Ca^{2+}]_o = 2$, $[A^-]_i = 187.5$, $[A^-]_o = 0$, $[HCO_3^-]_i = 15$, $[HCO_3^-]_o = 25$. These values gave the following Nernst potentials (in mV): $E_{Na} = 69.4$, $E_K = -84.5$, $E_{Cl} = -81.8$, $E_{Ca} = 139.3$, $E_{HCO3} = -13.4$, $E_{GABAa} = -69.5$.

Resting state

Steady-state conditions at rest were characterized by no net flux of the ions at the resting potential (-61 mV). These conditions were determined separately for each cell and compartment. For chloride, KCC2 cotransport strength U_{KCC2} was adjusted to balance Cl^- leak current at rest, i.e.:

$$I_{Cl,leak} = -I_{Cl,KCC2}$$

For sodium and potassium, first, Na^+ leak current conductance $g_{Na,leak}$ was adjusted to ensure that at rest all passive and voltage-gated membrane currents I_{Na} and I_K are in the ratio -3/2, i.e.,:

$$I_{Na} = -\frac{3}{2}I_K$$

Next, the Na^+/K^+-pump strength I_{max} was adjusted such that I_{Na} and I_K currents were balanced by equal and opposite pump currents:

$$-I_{Na} = I_{Na,pump}$$

$$-I_K = I_{K,Pump}$$

Synaptic connections and model inputs

The pyramidal cells created excitatory AMPA synaptic connections with the interneuron and all other pyramidal cells. The interneuron created an inhibitory $GABA_a$ synaptic connection with each pyramidal cell. Excitatory synapses were placed in the middle of the PY dendrite and the middle of the IN soma. Inhibitory synapses were placed in the middle of the PY soma. The time course of synaptic conductance was modelled with a built-in NEURON mechanism Exp2Syn, implementing a dual exponential function:

$$g = g_{max}\left[\exp\left(-\frac{t}{\tau_2}\right) - \exp\left(-\frac{t}{\tau_1}\right)\right]$$

where the rise and decay time constants, τ_1 and τ_2, were 2 ms and 6 ms, respectively, for all synapses. g_{max} = weight*factor, where the factor was defined so that the normalized peak was 1. The weights for the synapses between the PY and from the PY to the IN were w_{ee} = 0.0002 µS and w_{ei} = 0.0017 µS, respectively. The inhibitory synaptic weight, w_{ie}, was 0.0005 µS. All pyramidal cells received background input modelled as a Poisson spike train, which was different in each cell, activated an excitatory synapse at a rate of 5 Hz and had a synaptic weight w_{input} = 0.0004 µS. To initiate the SLE, a depolarizing ramp current, I_{inj}, was injected into the interneuron, with the initial amplitude of 0.35 nA linearly decreasing toward 0 over 40 seconds. The inhibitory $GABA_a$ postsynaptic currents were carried by Cl^- and HCO_3^- ions (Jedlicka et al., 2010):

$$I_{GABAa} = I_{Cl\,GABAa} + I_{HCO3\,GABAa}$$

$$I_{Cl\,GABAa} = (1-P)g(V - E_{Cl})$$

$$I_{HCO3\,GABAa} = Pg(V - E_{HCO3})$$

$$E_{GABAa} = (1-P)E_{Cl} + PE_{HCO3}$$

where relative permeability P was 0.18.

Calculation of the LFP

The local field potentials were calculated based on all transmembrane currents in all cells using the following equation (Nunez & Srinivasan, 2006):

$$\phi(r,t) = \frac{1}{4\pi\sigma}\sum_{n=1}^{N}\frac{I_n(t)}{|r - r_n|}$$

Where I_n is a point current source at position r_n (taken as the position of a mid-point of a compartment) and r is the position of the electrode. $\sigma =$ 0.3 S/m is the extracellular conductivity (Lindén et al., 2014). The electrode was located in the middle of the somatic layer of the PY and IN cells, approximately 16 um from the centers of the somas of two neighbouring PY cells. The currents from the interneuron were taken with a weight of 0.2 to decrease their contribution. Also, the influence of the injected current on the LFP was removed. The amplitude of the simulated LFP signal was an order of magnitude smaller than the experimental data. This was due to current point-source approximation and the small number of cells in the modeled network.

Inter-burst interval fitting

Inter-burst intervals were fitted in Matlab with linear, exponential, logarithmic and square root relationships. The linear function, $IBI(t) = A + Bt$, was fitted using the *polyfit* procedure. The exponential function, $IBI(t) = A+B\exp(Ct)$, was fitted using the *fminsearch* procedure. The logarithmic and square root fits were based on the bifurcation theory, which suggests that close to bifurcation, the oscillation frequency may be constant or decay as square root or inverse of a logarithm of the distance to the bifurcation (Izhikevich, 2000). Accordingly, we fitted IBI (i.e., inverse of frequency) with logarithmic and inverse square root functions $IBI(\lambda) = A + B\log(\lambda)$, where *log*() denotes the natural logarithm function, and $IBI(\lambda) = A + B/sqrt(\lambda)$, where *sqrt( )* denotes the square root function. Both functions were fitted using the *polyfit* procedure with $log(\lambda)$ and $1/sqrt(\lambda)$ treated as a predictor variable. The distance to the bifurcation point was computed as $\lambda = t_{end} - t + 1$, where t_{end} denotes bifurcation point, i.e., time of an SLE end while t is time since the beginning of an SLE. One second offset in λ was necessary to avoid infinity in the predictor variables when $t = t_{end}$. The goodness of fit was evaluated by Root Mean Square Error (RMSE).

Software Accessibility

If accepted, the model will be publicly available in the ModelDB (https://senselab.med.yale.edu/modeldb/)

Acknowledgements

We are grateful to Laura Uva and Laura Librizzi for helpful discussions throughout the preparation of this work and for providing the SLE data from the *in vitro* isolated whole guinea pig brain. We thank Laura Tassi from the *Claudio Munari* Epilepsy Surgery Center of the Niguarda Hospital in Milano, Italy, for providing the intracerebral data on human seizures. The work of MdC and VG was supported by the EPICARE grant of the Associazione Paolo Zorzi for the Neuroscience.

Competing interests

The authors report no competing interests.

References

Alfonsa, H., Merricks, E. M., Codadu, N. K., Cunningham, M. O., Deisseroth, K., Racca, C., & Trevelyan, A. J. (2015). The Contribution of Raised Intraneuronal Chloride to Epileptic Network Activity. *Journal of Neuroscience*, *35*(20), 7715–7726. https://doi.org/10.1523/JNEUROSCI.4105-14.2015

Andersen, P., Dingledine, R., Gjerstad, L., Langmoen, I. A., & Laursen, A. M. (1980). Two different responses of hippocampal pyramidal cells to application of gamma-amino butyric acid. *The Journal of Physiology*, *305*(1), 279–296. https://doi.org/10.1113/jphysiol.1980.sp013363

Aracri, P., de Curtis, M., Forcaia, G., & Uva, L. (2018). Enhanced thalamo-hippocampal synchronization during focal limbic seizures. *Epilepsia*, *59*(9), 1774–1784. https://doi.org/10.1111/epi.14521

Avoli, M., Barbarosie, M., Lücke, A., Nagao, T., Lopantsev, V., & Köhling, R. (1996). Synchronous GABA-Mediated Potentials and Epileptiform Discharges in the Rat Limbic System In Vitro. *The Journal of Neuroscience*, *16*(12), 3912–3924. https://doi.org/10.1523/JNEUROSCI.16-12-03912.1996

Avoli, M., De Curtis, M., Gnatkovsky, V., Gotman, J., Köhling, R., Lévesque, M., Manseau, F., Shiri, Z., & Williams, S. (2016). Specific imbalance of excitatory/inhibitory signaling establishes seizure onset pattern in temporal lobe epilepsy. *Journal of Neurophysiology*,

115(6), 3229–3237. https://doi.org/10.1152/jn.01128.2015

Bauer, P. R., Thijs, R. D., Lamberts, R. J., Velis, D. N., Visser, G. H., Tolner, E. A., Sander, J. W., Lopes da Silva, F. H., & Kalitzin, S. N. (2017). Dynamics of convulsive seizure termination and postictal generalized EEG suppression. *Brain*, *140*(3), 655–668. https://doi.org/10.1093/brain/aww322

Bazhenov, M., Timofeev, I., Steriade, M., & Sejnowski, T. J. (2004). Potassium model for slow (2-3 Hz) in vivo neocortical paroxysmal oscillations. *Journal of Neurophysiology*, *92*(2), 1116–1132. https://doi.org/10.1152/jn.00529.2003

Blauwblomme, T., Jiruska, P., & Huberfeld, G. (2014). Mechanisms of ictogenesis. In *International Review of Neurobiology* (Vol. 114, pp. 155–185). Academic Press Inc. https://doi.org/10.1016/B978-0-12-418693-4.00007-8

Boido, D., Gnatkovsky, V., Uva, L., Francione, S., & De Curtis, M. (2014). Simultaneous enhancement of excitation and postburst inhibition at the end of focal seizures. *Annals of Neurology*, *76*(6), 826–836. https://doi.org/10.1002/ana.24193

Borgdorff, J. A. (2002). *Calcium dynamics in hippocampal neurones* [University of Amsterdam]. https://hdl.handle.net/11245/1.201021

Bradford, H. F. (1995). Glutamate, GABA and epilepsy. *Progress in Neurobiology*, *47*(6), 477–511. https://doi.org/10.1016/0301-0082(95)00030-5

Bragin, A., Azizyan, A., Almajano, J., & Engel, J. (2009). The Cause of the Imbalance in the Neuronal Network Leading to Seizure Activity Can Be Predicted by the Electrographic Pattern of the Seizure Onset. *Journal of Neuroscience*, *29*(11), 3660–3671. https://doi.org/10.1523/JNEUROSCI.5309-08.2009

Bragin, Anatol, Penttonen, M., & Buzsáki, G. (1997). Termination of Epileptic Afterdischarge in the Hippocampus. *The Journal of Neuroscience*, *17*(7), 2567–2579. https://doi.org/10.1523/JNEUROSCI.17-07-02567.1997

Bromfield, E. B., Cavazos, J. E., & Sirven, J. I. (Eds.). (2006). *An Introduction to Epilepsy [Internet]*. West Hartford (CT): American Epilepsy Society.

https://www.ncbi.nlm.nih.gov/books/NBK2508/

Buchin, A., Chizhov, A., Huberfeld, G., Miles, R., & Gutkin, B. S. (2016). Reduced efficacy of the KCC2 cotransporter promotes epileptic oscillations in a subiculum network model. *Journal of Neuroscience*, *36*(46), 11619–11633. https://doi.org/10.1523/JNEUROSCI.4228-15.2016

Cherubini, E., Gaiarsa, J. L., & Ben-Ari, Y. (1991). GABA: an excitatory transmitter in early postnatal life. *Trends in Neurosciences*, *14*(12), 515–519. https://doi.org/10.1016/0166-2236(91)90003-D

Chizhov, A. V., Zefirov, A. V., Amakhin, D. V., Smirnova, E. Y., & Zaitsev, A. V. (2018). Minimal model of interictal and ictal discharges "Epileptor-2." *PLoS Computational Biology*, *14*(5), 1–25. https://doi.org/10.1371/journal.pcbi.1006186

Codadu, N. K., Graham, R. T., Burman, R. J., Jackson-Taylor, R. T., Raimondo, J. V., Trevelyan, A. J., & Parrish, R. R. (2019). Divergent paths to seizure-like events. *Physiological Reports*, *7*(19). https://doi.org/10.14814/phy2.14226

Conradsen, I., Moldovan, M., Jennum, P., Wolf, P., Farina, D., & Beniczky, S. (2013). Dynamics of muscle activation during tonic–clonic seizures. *Epilepsy Research*, *104*(1–2), 84–93. https://doi.org/10.1016/j.eplepsyres.2012.09.004

Cossart, R., Bernard, C., & Ben-Ari, Y. (2005). Multiple facets of GABAergic neurons and synapses: multiple fates of GABA signalling in epilepsies. *Trends in Neurosciences*, *28*(2), 108–115. https://doi.org/10.1016/j.tins.2004.11.011

de Curtis, M., & Avoli, M. (2016). GABAergic networks jump-start focal seizures. *Epilepsia*, *57*(5), 679–687. https://doi.org/10.1111/epi.13370

de Curtis, M., & Gnatkovsky, V. (2009). Reevaluating the mechanisms of focal ictogenesis: The role of low-voltage fast activity. *Epilepsia*, *50*(12), 2514–2525. https://doi.org/10.1111/j.1528-1167.2009.02249.x

de Curtis, M., Librizzi, L., & Uva, L. (2006). In Vitro Isolated Guinea Pig Brain. In A. Pitkänen, P. A. Schwartzkroin, & S. L. Moshé (Eds.), *Models of Seizures and Epilepsy*

(pp. 103–109). Academic Press Inc. https://doi.org/10.1016/B978-012088554-1/50011-6

de Curtis, M., Uva, L., Gnatkovsky, V., & Librizzi, L. (2018). Potassium dynamics and seizures: Why is potassium ictogenic? *Epilepsy Research*, *143*(April), 50–59. https://doi.org/10.1016/j.eplepsyres.2018.04.005

Derchansky, M., Jahromi, S. S., Mamani, M., Shin, D. S., Sik, A., & Carlen, P. L. (2008). Transition to seizures in the isolated immature mouse hippocampus: a switch from dominant phasic inhibition to dominant phasic excitation. *The Journal of Physiology*, *586*(2), 477–494. https://doi.org/10.1113/jphysiol.2007.143065

Devinsky, O., Vezzani, A., O'Brien, T. J., Jette, N., Scheffer, I. E., de Curtis, M., & Perucca, P. (2018). Epilepsy. *Nature Reviews Disease Primers*, *4*(1), 18024. https://doi.org/10.1038/nrdp.2018.24

Dietzel, I., Heinemann, U., Hofmeier, G., & Lux, H. D. (1980). Transient changes in the size of the extracellular space in the sensorimotor cortex of cats in relation to stimulus-induced changes in potassium concentration. *Experimental Brain Research*, *40*(4). https://doi.org/10.1007/BF00236151

Dietzel, I., Heinemann, U., Hofmeier, G., & Lux, H. D. (1982). Stimulus-induced changes in extracellular Na+ and Cl- concentration in relation to changes in the size of the extracellular space. *Experimental Brain Research*, *46*(1), 73–84. https://doi.org/10.1007/BF00238100

Doyon, N., Prescott, S. A., Castonguay, A., Godin, A. G., Kröger, H., & De Koninck, Y. (2011). Efficacy of Synaptic Inhibition Depends on Multiple, Dynamically Interacting Mechanisms Implicated in Chloride Homeostasis. *PLoS Computational Biology*, *7*(9), e1002149. https://doi.org/10.1371/journal.pcbi.1002149

During, M. J., & Spencer, D. D. (1992). Adenosine: A potential mediator of seizure arrest and postictal refractoriness. *Annals of Neurology*, *32*(5), 618–624. https://doi.org/10.1002/ana.410320504

Ebert, U., Cramer, S., & Löscher, W. (1997). Phenytoin's effect on the spread of seizure activity in the amygdala kindling model. *Naunyn-Schmiedeberg's Archives of*

Pharmacology, *356*(3), 341–347. https://doi.org/10.1007/PL00005060

Elahian, B., Lado, N. E., Mankin, E., Vangala, S., Misra, A., Moxon, K., Fried, I., Sharan, A., Yeasin, M., Staba, R., Bragin, A., Avoli, M., Sperling, M. R., Engel, J., & Weiss, S. A. (2018). Low-voltage fast seizures in humans begin with increased interneuron firing. *Annals of Neurology*, *84*(4), 588–600. https://doi.org/10.1002/ana.25325

Ellender, T. J., Raimondo, J. V., Irkle, A., Lamsa, K. P., & Akerman, C. J. (2014). Excitatory effects of parvalbumin-expressing interneurons maintain hippocampal epileptiform activity via synchronous afterdischarges. *Journal of Neuroscience*, *34*(46), 15208–15222. https://doi.org/10.1523/JNEUROSCI.1747-14.2014

Evangelista, E., Bénar, C., Bonini, F., Carron, R., Colombet, B., Régis, J., & Bartolomei, F. (2015). Does the Thalamo-Cortical Synchrony Play a Role in Seizure Termination? *Frontiers in Neurology*, *6*. https://doi.org/10.3389/fneur.2015.00192

Feng, Z., & Durand, D. M. (2003). Low-Calcium Epileptiform Activity in the Hippocampus In Vivo. *Journal of Neurophysiology*, *90*(4), 2253–2260. https://doi.org/10.1152/jn.00241.2003

Fisher, R. S., Pedley, T. A., Moody, W. J., & Prince, D. A. (1976). The Role of Extracellular Potassium in Hippocampal Epilepsy. *Archives of Neurology*, *33*(2), 76–83. https://doi.org/10.1001/archneur.1976.00500020004002

Fisher, Robert S., & Schachter, S. C. (2000). The Postictal State: A Neglected Entity in the Management of Epilepsy. *Epilepsy and Behavior*, *1*(1), 52–59. https://doi.org/10.1006/ebeh.2000.0023

Franaszczuk, P. J., Bergey, G. K., Durka, P. J., & Eisenberg, H. M. (1998). Time-frequency analysis using the matching pursuit algorithm applied to seizures originating from the mesial temporal lobe. *Electroencephalography and Clinical Neurophysiology*, *106*(6), 513–521. https://doi.org/10.1016/S0013-4694(98)00024-8

Fransen, E., Alonso, A. A., & Hasselmo, M. E. (2002). Simulations of the role of the muscarinic-activated calcium-sensitive nonspecific cation current INCM in entorhinal neuronal activity during delayed matching tasks. *Journal of Neuroscience*, *22*(3), 1081–

1097. https://doi.org/10.1523/jneurosci.22-03-01081.2002

Fröhlich, F., Bazhenov, M., Timofeev, I., Steriade, M., & Sejnowski, T. J. (2006). Slow state transitions of sustained neural oscillations by activity-dependent modulation of intrinsic excitability. *Journal of Neuroscience*, *26*(23), 6153–6162. https://doi.org/10.1523/JNEUROSCI.5509-05.2006

Fujiwara-Tsukamoto, Y., Isomura, Y., Imanishi, M., Fukai, T., & Takada, M. (2007). Distinct types of ionic modulation of GABA actions in pyramidal cells and interneurons during electrical induction of hippocampal seizure-like network activity. *European Journal of Neuroscience*, *25*(9), 2713–2725. https://doi.org/10.1111/j.1460-9568.2007.05543.x

Futamachi, K. J., Mutani, R., & Prince, D. A. (1974). Potassium activity in rabbit cortex. *Brain Research*, *75*(1), 5–25. https://doi.org/10.1016/0006-8993(74)90767-7

Gentiletti, D., Suffczynski, P., Gnatkovsky, V., & De Curtis, M. (2017). Changes of Ionic Concentrations during Seizure Transitions-A Modeling Study. *International Journal of Neural Systems*, *27*(4), 1–16. https://doi.org/10.1142/S0129065717500046

Gnatkovsky, V., Librizzi, L., Trombin, F., & De Curtis, M. (2008). Fast activity at seizure onset is mediated by inhibitory circuits in the entorhinal cortex in vitro. *Annals of Neurology*, *64*(6), 674–686. https://doi.org/10.1002/ana.21519

Golomb, D., Yue, C., & Yaari, Y. (2006). Contribution of Persistent Na + Current and M-Type K + Current to Somatic Bursting in CA1 Pyramidal Cells: Combined Experimental and Modeling Study. *Journal of Neurophysiology*, *96*(4), 1912–1926. https://doi.org/10.1152/jn.00205.2006

González, O. C., Shiri, Z., Krishnan, G. P., Myers, T. L., Williams, S., Avoli, M., & Bazhenov, M. (2018). Role of KCC2-dependent potassium efflux in 4-Aminopyridine-induced Epileptiform synchronization. *Neurobiology of Disease*, *109*(August 2017), 137–147. https://doi.org/10.1016/j.nbd.2017.10.011

Grasse, D. W., Karunakaran, S., & Moxon, K. A. (2013). Neuronal synchrony and the transition to spontaneous seizures. *Experimental Neurology*, *248*, 72–84. https://doi.org/10.1016/j.expneurol.2013.05.004

Grigorovsky, V., Jacobs, D., Breton, V. L., Tufa, U., Lucasius, C., del Campo, J. M., Chinvarun, Y., Carlen, P. L., Wennberg, R., & Bardakjian, B. L. (2020). Delta-gamma phase-amplitude coupling as a biomarker of postictal generalized EEG suppression. *Brain Communications*, *2*(2). https://doi.org/10.1093/braincomms/fcaa182

Haas, H. L., & Jefferys, J. G. (1984). Low-calcium field burst discharges of CA1 pyramidal neurones in rat hippocampal slices. *The Journal of Physiology*, *354*(1), 185–201. https://doi.org/10.1113/jphysiol.1984.sp015371

Hamidi, S., & Avoli, M. (2015). KCC2 function modulates in vitro ictogenesis. *Neurobiology of Disease*, *79*, 51–58. https://doi.org/10.1016/j.nbd.2015.04.006

Heinemann, U., Lux, H. D., & Gutnick, M. J. (1977). Extracellular free calcium and potassium during paroxysmal activity in the cerebral cortex of the cat. *Experimental Brain Research*, *27*(3–4), 237–243. https://doi.org/10.1007/BF00235500

Heinemann, Uwe, & Lux, H. D. (1975). Undershoots following stimulus-induced rises of extracellular potassium concentration in cerebral cortex of cat. *Brain Research*, *93*(1), 63–76. https://doi.org/10.1016/0006-8993(75)90286-3

Ho, Y. E. C., & Truccolo, W. (2016). Interaction between synaptic inhibition and glial-potassium dynamics leads to diverse seizure transition modes in biophysical models of human focal seizures. *Journal of Computational Neuroscience*, *41*(2), 225–244. https://doi.org/10.1007/s10827-016-0615-7

Hübel, N., & Ullah, G. (2016). Anions Govern Cell Volume: A Case Study of Relative Astrocytic and Neuronal Swelling in Spreading Depolarization. *PLOS ONE*, *11*(3), e0147060. https://doi.org/10.1371/journal.pone.0147060

Igelström, K. M. (2013). Is Slack an Intrinsic Seizure Terminator? *The Neuroscientist*, *19*(3), 248–254. https://doi.org/10.1177/1073858412446311

IZHIKEVICH, E. M. (2000). NEURAL EXCITABILITY, SPIKING AND BURSTING. *International Journal of Bifurcation and Chaos*, *10*(06), 1171–1266. https://doi.org/10.1142/S0218127400000840

Jedlicka, P., Deller, T., Gutkin, B. S., & Backus, K. H. (2010). Activity-dependent intracellular chloride accumulation and diffusion controls GABAA receptor-mediated synaptic transmission. *Hippocampus*, n/a-n/a. https://doi.org/10.1002/hipo.20804

Jefferys, J. G. (1995). Nonsynaptic modulation of neuronal activity in the brain: electric currents and extracellular ions. *Physiological Reviews*, *75*(4), 689–723. https://doi.org/10.1152/physrev.1995.75.4.689

Jefferys, J. G. R., & Haas, H. L. (1982). Synchronized bursting of CA1 hippocampal pyramidal cells in the absence of synaptic transmission. *Nature*, *300*(5891), 448–450. https://doi.org/10.1038/300448a0

Jefferys, J., Jiruska, P., de Curtis, M., & Avoli, M. (2012). Limbic Network Synchronization and Temporal Lobe Epilepsy. In J. Noebels, M. Avoli, M. Rogawski, R. Olsen, & A. Delgado-Escueta (Eds.), *Jasper's Basic Mechanisms of the Epilepsies*. Bethesda (MD): National Center for Biotechnology Information (US). http://www.ncbi.nlm.nih.gov/pubmed/22787650

Jensen, M. S., & Yaari, Y. (1997). Role of intrinsic burst firing, potassium accumulation, and electrical coupling in the elevated potassium model of hippocampal epilepsy. *Journal of Neurophysiology*, *77*(3), 1224–1233. https://doi.org/10.1152/jn.1997.77.3.1224

Jirsa, V. K., Stacey, W. C., Quilichini, P. P., Ivanov, A. I., & Bernard, C. (2014). On the nature of seizure dynamics. *Brain*, *137*(8), 2210–2230. https://doi.org/10.1093/brain/awu133

Kager, H., Wadman, W. J., & Somjen, G. G. (2000). Simulated Seizures and Spreading Depression in a Neuron Model Incorporating Interstitial Space and Ion Concentrations. *Journal of Neurophysiology*, *84*(1), 495–512. https://doi.org/10.1152/jn.2000.84.1.495

Kager, H., Wadman, W. J., & Somjen, G. G. (2002). Conditions for the triggering of spreading depression studied with computer simulations. *Journal of Neurophysiology*, *88*(5), 2700–2712. https://doi.org/10.1152/jn.00237.2002

Kaila, K., Lamsa, K., Smirnov, S., Taira, T., & Voipio, J. (1997). Long-lasting GABA-mediated depolarization evoked by high-frequency stimulation in pyramidal neurons of rat hippocampal slice is attributable to a network-driven, bicarbonate-dependent K+

transient. *Journal of Neuroscience*, *17*(20), 7662–7672. https://doi.org/10.1523/jneurosci.17-20-07662.1997

Kaila, K., Price, T. J., Payne, J. A., Puskarjov, M., & Voipio, J. (2014). Cation-chloride cotransporters in neuronal development, plasticity and disease. *Nature Reviews Neuroscience*, *15*(10), 637–654. https://doi.org/10.1038/nrn3819

Kalitzin, S. N., Bauer, P. R., Lamberts, R. J., Velis, D. N., Thijs, R. D., & Da Silva, F. H. L. (2016). Automated Video Detection of Epileptic Convulsion Slowing as a Precursor for Post-Seizure Neuronal Collapse. *International Journal of Neural Systems*, *26*(8), 100–104. https://doi.org/10.1142/S0129065716500271

Krishnan, G. P., & Bazhenov, M. (2011). Ionic dynamics mediate spontaneous termination of seizures and postictal depression state. *Journal of Neuroscience*, *31*(24), 8870–8882. https://doi.org/10.1523/JNEUROSCI.6200-10.2011

Krishnan, G. P., Filatov, G., Shilnikov, A., & Bazhenov, M. (2015). Electrogenic properties of the Na+/K+ ATPase control transitions between normal and pathological brain states. *Journal of Neurophysiology*, *113*(9), 3356–3374. https://doi.org/10.1152/jn.00460.2014

Lado, F. A., & Moshé, S. L. (2008). How do seizures stop? *Epilepsia*, *49*(10), 1651–1664. https://doi.org/10.1111/j.1528-1167.2008.01669.x

Lagarde, S., Buzori, S., Trebuchon, A., Carron, R., Scavarda, D., Milh, M., McGonigal, A., & Bartolomei, F. (2019). The repertoire of seizure onset patterns in human focal epilepsies: Determinants and prognostic values. *Epilepsia*, *60*(1), 85–95. https://doi.org/10.1111/epi.14604

Lévesque, M., Herrington, R., Hamidi, S., & Avoli, M. (2016). Interneurons spark seizure-like activity in the entorhinal cortex. *Neurobiology of Disease*, *87*, 91–101. https://doi.org/10.1016/j.nbd.2015.12.011

Lian, J., Bikson, M., Shuai, J., & Durand, D. M. (2001). Propagation of non-synaptic epileptiform activity across a lesion in rat hippocampal slices. *Journal of Physiology*, *537*(1), 191–199. https://doi.org/10.1111/j.1469-7793.2001.0191k.x

Lillis, K. P., Kramer, M. A., Mertz, J., Staley, K. J., & White, J. A. (2012). Pyramidal cells accumulate chloride at seizure onset. *Neurobiology of Disease*, *47*(3), 358–366. https://doi.org/10.1016/j.nbd.2012.05.016

Lindén, H., Hagen, E., Łeski, S., Norheim, E. S., Pettersen, K. H., & Einevoll, G. T. (2014). LFPy: A tool for biophysical simulation of extracellular potentials generated by detailed model neurons. *Frontiers in Neuroinformatics*, *7*(JAN), 1–15. https://doi.org/10.3389/fninf.2013.00041

Liou, J., Smith, E. H., Bateman, L. M., Bruce, S. L., McKhann, G. M., Goodman, R. R., Emerson, R. G., Schevon, C. A., & Abbott, L. (2020). A model for focal seizure onset, propagation, evolution, and progression. *ELife*, *9*. https://doi.org/10.7554/eLife.50927

Lopantsev, V., & Avoli, M. (1998). Participation of GABA(A)-mediated inhibition in ictallike discharges in the rat entorhinal cortex. *Journal of Neurophysiology*, *79*(1), 352–360. https://doi.org/10.1152/jn.1998.79.1.352

Magistretti, J., & Alonso, A. (1999). Biophysical Properties and Slow Voltage-Dependent Inactivation of a Sustained Sodium Current in Entorhinal Cortex Layer-II Principal Neurons. *Journal of General Physiology*, *114*(4), 491–509. https://doi.org/10.1085/jgp.114.4.491

Magloire, V., Cornford, J., Lieb, A., Kullmann, D. M., & Pavlov, I. (2019). KCC2 overexpression prevents the paradoxical seizure-promoting action of somatic inhibition. *Nature Communications*, *10*(1), 1–13. https://doi.org/10.1038/s41467-019-08933-4

Magloire, V., Mercier, M. S., Kullmann, D. M., & Pavlov, I. (2019). GABAergic Interneurons in Seizures: Investigating Causality With Optogenetics. *The Neuroscientist*, *25*(4), 344–358. https://doi.org/10.1177/1073858418805002

Martinet, L.-E., Fiddyment, G., Madsen, J. R., Eskandar, E. N., Truccolo, W., Eden, U. T., Cash, S. S., & Kramer, M. A. (2017). Human seizures couple across spatial scales through travelling wave dynamics. *Nature Communications*, *8*(1), 14896. https://doi.org/10.1038/ncomms14896

McBain, C., Traynelis, S., & Dingledine, R. (1990). Regional variation of extracellular space

in the hippocampus. *Science*, *249*(4969), 674–677. https://doi.org/10.1126/science.2382142

Miles, R., Blaesse, P., Huberfeld, G., Wittner, L., & Kaila, K. (2012). Chloride homeostasis and GABA signaling in temporal lobe epilepsy. In D.-E. A. Noebels JL, Avoli M, Rogawski MA, Olsen RW (Ed.), *Jasper's Basic Mechanisms of the Epilepsies*. National Center for Biotechnology Information (US). http://www.ncbi.nlm.nih.gov/pubmed/22787654

Miri, M. L., Vinck, M., Pant, R., & Cardin, J. A. (2018). Altered hippocampal interneuron activity precedes ictal onset. *ELife*, *7*. https://doi.org/10.7554/eLife.40750

Moore, Y. E., Deeb, T. Z., Chadchankar, H., Brandon, N. J., & Moss, S. J. (2018). Potentiating KCC2 activity is sufficient to limit the onset and severity of seizures. *Proceedings of the National Academy of Sciences of the United States of America*, *115*(40), 10166–10171. https://doi.org/10.1073/pnas.1810134115

Nunez, P. L., & Srinivasan, R. (2006). *Electric Fields of the Brain*. Oxford University Press. https://doi.org/10.1093/acprof:oso/9780195050387.001.0001

Payne, D. E., Karoly, P. J., Freestone, D. R., Boston, R., D'Souza, W., Nurse, E., Kuhlmann, L., Cook, M. J., & Grayden, D. B. (2018). Postictal suppression and seizure durations: A patient-specific, long-term iEEG analysis. *Epilepsia*, *59*(5), 1027–1036. https://doi.org/10.1111/epi.14065

Payne, J. A. (1997). Functional characterization of the neuronal-specific K-Cl cotransporter: Implications for [K+](o) regulation. *American Journal of Physiology - Cell Physiology*, *273*(5 42-5). https://doi.org/10.1152/ajpcell.1997.273.5.c1516

Payne, J. A., Rivera, C., Voipio, J., & Kaila, K. (2003). Cation-chloride co-transporters in neuronal communication, development and trauma. *Trends in Neurosciences*, *26*(4), 199–206. https://doi.org/10.1016/S0166-2236(03)00068-7

Perucca, P., Dubeau, F., & Gotman, J. (2014). Intracranial electroencephalographic seizure-onset patterns: effect of underlying pathology. *Brain*, *137*(1), 183–196. https://doi.org/10.1093/brain/awt299

Pottkämper, J. C. M., Hofmeijer, J., van Waarde, J. A., & van Putten, M. J. A. M. (2020). The postictal state — What do we know? *Epilepsia*, *61*(6), 1045–1061. https://doi.org/10.1111/epi.16519

Proix, T., Jirsa, V. K., Bartolomei, F., Guye, M., & Truccolo, W. (2018). Predicting the spatiotemporal diversity of seizure propagation and termination in human focal epilepsy. *Nature Communications*, *9*(1), 1088. https://doi.org/10.1038/s41467-018-02973-y

Pumain, R., Menini, C., Heinemann, U., Louvel, J., & Silva-Barrat, C. (1985). Chemical synaptic transmission is not necessary for epileptic seizures to persist in the baboon Papio papio. *Experimental Neurology*, *89*(1), 250–258. https://doi.org/10.1016/0014-4886(85)90280-8

Raimondo, J. (2013). A genetically-encoded chloride and pH sensor for dissociating ion dynamics in the nervous system. *Frontiers in Cellular Neuroscience*, *7*. https://doi.org/10.3389/fncel.2013.00202

Raimondo, J. V., Burman, R. J., Katz, A. A., & Akerman, C. J. (2015). Ion dynamics during seizures. *Frontiers in Cellular Neuroscience*, *9*, 1–14. https://doi.org/10.3389/fncel.2015.00419

Rich, S., Chameh, H. M., Rafiee, M., Ferguson, K., Skinner, F. K., & Valiante, T. A. (2020). Inhibitory Network Bistability Explains Increased Interneuronal Activity Prior to Seizure Onset. *Frontiers in Neural Circuits*, *13*. https://doi.org/10.3389/fncir.2019.00081

Saggio, M. L., Crisp, D., Scott, J. M., Karoly, P., Kuhlmann, L., Nakatani, M., Murai, T., Dümpelmann, M., Schulze-Bonhage, A., Ikeda, A., Cook, M., Gliske, S. V, Lin, J., Bernard, C., Jirsa, V., & Stacey, W. C. (2020). A taxonomy of seizure dynamotypes. *ELife*, *9*. https://doi.org/10.7554/eLife.55632

Salami, P., Borzello, M., Kramer, M. A., Westover, M. B., & Cash, S. S. (2022). Quantifying seizure termination patterns reveals limited pathways to seizure end. *Neurobiology of Disease*, *165*, 105645. https://doi.org/10.1016/j.nbd.2022.105645

Schiff, S. J., Colella, D., Jacyna, G. M., Hughes, E., Creekmore, J. W., Marshall, A., Bozek-Kuzmicki, M., Benke, G., Gaillard, W. D., Conry, J., & Weinstein, S. R. (2000). Brain

chirps: spectrographic signatures of epileptic seizures. *Clinical Neurophysiology*, *111*(6), 953–958. https://doi.org/10.1016/S1388-2457(00)00259-5

Schindler, K., Leung, H., Elger, C. E., & Lehnertz, K. (2007). Assessing seizure dynamics by analysing the correlation structure of multichannel intracranial EEG. *Brain*, *130*(1), 65–77. https://doi.org/10.1093/brain/awl304

Shivacharan, R. S., Chiang, C.-C., Zhang, M., Gonzalez-Reyes, L. E., & Durand, D. M. (2019). Self-propagating, non-synaptic epileptiform activity recruits neurons by endogenous electric fields. *Experimental Neurology*, *317*, 119–128. https://doi.org/10.1016/j.expneurol.2019.02.005

Somjen, G. G., & Giacchino, J. L. (1985). Potassium and calcium concentrations in interstitial fluid of hippocampal formation during paroxysmal responses. *Journal of Neurophysiology*, *53*(4), 1098–1108. https://doi.org/10.1152/jn.1985.53.4.1098

Somjen, G. G., Kager, H., & Wadman, W. J. (2008). Computer simulations of neuron-glia interactions mediated by ion flux. *Journal of Computational Neuroscience*, *25*(2), 349–365. https://doi.org/10.1007/s10827-008-0083-9

Spencer, S. S., Guimaraes, P., Katz, A., Kim, J., & Spencer, D. (1992). Morphological Patterns of Seizures Recorded Intracranially. *Epilepsia*, *33*(3), 537–545. https://doi.org/10.1111/j.1528-1157.1992.tb01706.x

Staley, K. J., & Proctor, W. R. (1999). Modulation of mammalian dendritic GABA A receptor function by the kinetics of Cl − and HCO 3 − transport. *The Journal of Physiology*, *519*(3), 693–712. https://doi.org/10.1111/j.1469-7793.1999.0693n.x

Staley, K. J., Soldo, B. L., & Proctor, W. R. (1995). Ionic Mechanisms of Neuronal Excitation by Inhibitory GABA A Receptors. *Science*, *269*(5226), 977–981. https://doi.org/10.1126/science.7638623

Suffczynski, P., Gentiletti, D., Gnatkovsky, V., & de Curtis, M. (2017). Extracellular Potassium and Focal Seizures—Insight from In Silico Study. In P. Érdi, B. Sen Bhattacharya, & A. Cochran (Eds.), *Computational Neurology and Psychiatry. Springer Series in Bio-/Neuroinformatics* (pp. 49–72). Springer, Cham.

https://doi.org/10.1007/978-3-319-49959-8_3

Sulis Sato, S., Artoni, P., Landi, S., Cozzolino, O., Parra, R., Pracucci, E., Trovato, F., Szczurkowska, J., Luin, S., Arosio, D., Beltram, F., Cancedda, L., Kaila, K., & Ratto, G. M. (2017). Simultaneous two-photon imaging of intracellular chloride concentration and pH in mouse pyramidal neurons in vivo. *Proceedings of the National Academy of Sciences*, *114*(41), E8770–E8779. https://doi.org/10.1073/pnas.1702861114

Theparambil, S. M., Hosford, P. S., Ruminot, I., Kopach, O., Reynolds, J. R., Sandoval, P. Y., Rusakov, D. A., Barros, L. F., & Gourine, A. V. (2020). Astrocytes regulate brain extracellular pH via a neuronal activity-dependent bicarbonate shuttle. *Nature Communications*, *11*(1), 5073. https://doi.org/10.1038/s41467-020-18756-3

Thompson, S. M., & Gahwiler, B. H. (1989). Activity-dependent disinhibition. II. Effects of extracellular potassium, furosemide, and membrane potential on ECl- in hippocampal CA3 neurons. *Journal of Neurophysiology*, *61*(3), 512–523. https://doi.org/10.1152/jn.1989.61.3.512

Timofeev, I., & Steriade, M. (2004). Neocortical seizures: initiation, development and cessation. *Neuroscience*, *123*(2), 299–336. https://doi.org/10.1016/j.neuroscience.2003.08.051

Toyoda, I., Fujita, S., Thamattoor, A. K., & Buckmaster, P. S. (2015). Unit Activity of Hippocampal Interneurons before Spontaneous Seizures in an Animal Model of Temporal Lobe Epilepsy. *Journal of Neuroscience*, *35*(16), 6600–6618. https://doi.org/10.1523/JNEUROSCI.4786-14.2015

Traub, R. D., Buhl, E. H., Gloveli, T., & Whittington, M. A. (2003). Fast Rhythmic Bursting Can Be Induced in Layer 2/3 Cortical Neurons by Enhancing Persistent Na + Conductance or by Blocking BK Channels. *Journal of Neurophysiology*, *89*(2), 909–921. https://doi.org/10.1152/jn.00573.2002

Traynelis, S. F., & Dingledine, R. (1988). Potassium-induced spontaneous electrographic seizures in the rat hippocampal slice. *Journal of Neurophysiology*, *59*(1), 259–276. https://doi.org/10.1152/jn.1988.59.1.259

Truccolo, W., Donoghue, J. A., Hochberg, L. R., Eskandar, E. N., Madsen, J. R., Anderson, W. S., Brown, E. N., Halgren, E., & Cash, S. S. (2011). Single-neuron dynamics in human focal epilepsy. *Nature Neuroscience*, *14*(5), 635–643. https://doi.org/10.1038/nn.2782

Uva, L., Breschi, G. L., Gnatkovsky, V., Taverna, S., & de Curtis, M. (2015). Synchronous inhibitory potentials precede seizure-like events in acute models of focal limbic seizures. *Journal of Neuroscience*, *35*(7), 3048–3055. https://doi.org/10.1523/JNEUROSCI.3692-14.2015

Uva, L., & de Curtis, M. (2020). Activity- and pH-dependent adenosine shifts at the end of a focal seizure in the entorhinal cortex. *Epilepsy Research*, *165*, 106401. https://doi.org/10.1016/j.eplepsyres.2020.106401

Velascol, A. L., Wilson, C. L., Babb, T. L., & Engel Jr, J. (2000). Functional and Anatomic Correlates of Two Frequently Observed Temporal Lobe Seizure-Onset Patterns. *Neural Plasticity*, *7*(1–2), 49–63. https://doi.org/10.1155/NP.2000.49

Viitanen, T., Ruusuvuori, E., Kaila, K., & Voipio, J. (2010). The K+-Cl- cotransporter KCC2 promotes GABAergic excitation in the mature rat hippocampus. *Journal of Physiology*, *588*(9), 1527–1540. https://doi.org/10.1113/jphysiol.2009.181826

Wei, Y., Ullah, G., Ingram, J., & Schiff, S. J. (2014). Oxygen and seizure dynamics: II. Computational modeling. *Journal of Neurophysiology*, *112*(2), 213–223. https://doi.org/10.1152/jn.00541.2013

Wei, Y., Ullah, G., & Schiff, S. J. (2014). Unification of neuronal spikes, seizures, and spreading depression. *Journal of Neuroscience*, *34*(35), 11733–11743. https://doi.org/10.1523/JNEUROSCI.0516-14.2014

Wen, B., Qian, H., Feng, J., Ge, R.-J., Xu, X., Cui, Z.-Q., Zhu, R.-Y., Pan, L.-S., Lin, Z.-P., & Wang, J.-H. (2015). A Portion of Inhibitory Neurons in Human Temporal Lobe Epilepsy are Functionally Upregulated: An Endogenous Mechanism for Seizure Termination. *CNS Neuroscience & Therapeutics*, *21*(2), 204–214. https://doi.org/10.1111/cns.12336

Yaari, Y., Konnerth, A., & Heinemann, U. (1983). Spontaneous epileptiform activity of ca1 hippocampal neurons in low extracellular calcium solutions. *Experimental Brain*

Research, *51*(1). https://doi.org/10.1007/BF00236813

Yekhlef, L., Breschi, G. L., Lagostena, L., Russo, G., & Taverna, S. (2015). Selective activation of parvalbumin- or somatostatin-expressing interneurons triggers epileptic seizurelike activity in mouse medial entorhinal cortex. *Journal of Neurophysiology*, *113*(5), 1616–1630. https://doi.org/10.1152/jn.00841.2014

Ziburkus, J., Cressman, J. R., Barreto, E., & Schiff, S. J. (2006). Interneuron and pyramidal cell interplay during in vitro seizure-like events. *Journal of Neurophysiology*, *95*(6), 3948–3954. https://doi.org/10.1152/jn.01378.2005

Ziemann, A. E., Schnizler, M. K., Albert, G. W., Severson, M. A., Howard III, M. A., Welsh, M. J., & Wemmie, J. A. (2008). Seizure termination by acidosis depends on ASIC1a. *Nature Neuroscience*, *11*(7), 816–822. https://doi.org/10.1038/nn.2132

Zubler, F., Steimer, A., Gast, H., & Schindler, K. A. (2014). Seizure Termination. In *International Review of Neurobiology* (pp. 187–207). Academic Press Inc. https://doi.org/10.1016/B978-0-12-418693-4.00008-X

Figure legends

Figure 1. Model diagram. The model consisted of four pyramidal cells (orange) and an interneuron (green) linked by excitatory (AMPA) and inhibitory (GABAa) synaptic connections. Each cellular compartment was surrounded by an interstitial compartment. The interstitial space was enclosed in a common bath (blue) which represented the surrounding tissue and vasculature not included in the model. The model included variable intracellular and extracellular ion concentrations computed according to ionic currents flowing across neuronal membranes, longitudinal diffusion between the dendritic and somatic compartments, radial diffusion between neighboring interstitial compartments and diffusion to/from the bath. Additionally, the model included ionic regulation mechanisms: a Na^+/K^+-pump, a KCC2 cotransporter and K^+ buffering by astrocytes.

Figure 2. Model behavior during an SLE. (A) Local field potential (LFP) signal. **(B)** Pyramidal cell (PY) membrane potential. **(C)** Interneuron (IN) membrane potential. **(D)**

1445 Extracellular potassium concentration. **(E)** Intracellular sodium concentration. **(F)** Intracellular
1446 chloride concentration. In the interictal phase (0–60 seconds), the model generated irregular
1447 background firing and the ion concentrations were at their resting values (**A–F**). The current
1448 injected into the interneuron at second 60 (**C**, yellow) triggered fast IN spiking (**C**, black) which
1449 also manifested as low voltage fast activity in the LFP signal (**A**). Approximately 10 seconds
1450 after the initiation of the SLE, PY cells initiated tonic firing that subsequently shifted to bursting
1451 (**B**). The behavior of the PY cells was reflected in the LFP trace which showed irregular activity
1452 and synchronized bursting (**A**). The SLE terminated at approximately second 120 and was
1453 followed by a period of reduced excitability (**A–C**). The cellular activity was accompanied by
1454 significant ion concentration shifts. Extracellular potassium in the somatic compartment
1455 increased sharply and remained elevated throughout the SLE (**D**, dark blue). The $[K^+]_o$ increase
1456 in the dendritic compartment was slower and less pronounced (**D**, violet). The intracellular
1457 sodium increased gradually toward a plateau (**E**). The intracellular chloride accumulated steadily
1458 throughout the SLE (**F**).

1459 **Figure 3. A comparison between the experimental data and the model simulation. (A)**
1460 Experimental recordings of a seizure-like event (SLE) in the *in vitro* isolated whole guinea pig
1461 brain preparation (de Curtis et al., 2006; Gnatkovsky et al., 2008; Uva et al., 2015). From top to
1462 bottom: LFP signal, intracellular recording of pyramidal cell (PY) and interneuron (IN),
1463 extracellular potassium. The onset of the SLE was associated with increased IN firing, silencing
1464 PY and low-voltage fast (LVF) activity in the LFP signal. Approximately 10 seconds after the
1465 onset of the SLE, the PY exhibited a tonic and then burst firing behavior. The extracellular
1466 potassium increased up to approximately 10 mM at the onset of the SLE and remained elevated
1467 afterward. **(B)** The activity patterns in the LFP signal, pyramidal cells, interneuron and $[K^+]_o$
1468 were reproduced accurately by the model. Signals presented in Figure 3a were recorded in
1469 different experiments. LFP and interneuron data have been published previously (Gentiletti et
1470 al., 2017; Gnatkovsky et al., 2008) while pyramidal cell and $[K^+]_o$ data have never been published
1471 before.

1472 **Figure 4. Analysis of the model.** In the bifurcation analysis extracellular potassium and
1473 intracellular sodium concentrations in the PY and IN cells were control parameters.
1474 Concentrations of all other ions were fixed at their reference values (except chloride: $[Cl^-]_{i,soma}$,
1475 $[Cl^-]_{i,dend}$ equal to 7 mM), all ion accumulation mechanisms were blocked and background input
1476 was removed. **(A)** Bifurcation diagrams showing the dependence of the behavior of the model

on $[K^+]_{o,dend}$ and $[K^+]_{o,soma}$ for varying values of $[Na^+]_{i,soma}$, $[Na^+]_{i,dend}$. The diagram colors correspond to types of activity shown on the right: rest (yellow), tonic firing (violet) and bursting (dark blue). An increase in $[Na^+]_i$ progressively decreased the domains of tonic firing and bursting and increased the resting domain indicating a general decrease in network excitability. The black and gray arrows correspond to the evolution of $[K^+]_{o,soma}$, $[K^+]_{o,dend}$ during different phases of the SLE, shown in part **B**. **(B)** A simulation of the model with $[K^+]_{o,soma}$, $[K^+]_{o,dend}$ and $[Na^+]_{i,soma}$, $[Na^+]_{i,dend}$ as the external control parameters, that illustrated the occurrence of transitions between different types of activity during the SLE. The top two panels show the time course of $[K^+]_{o,soma}$, $[K^+]_{o,dend}$ and $[Na^+]_{i,soma}$, $[Na^+]_{i,dend}$ and approximate their evolution during the SLE (Figure 2). The third panel shows the resulting PY cell behavior. The parameter evolution is divided into four phases indicated by the arrows denoted as I–IV in part **A** and **B**. Phase I corresponds to a sharp increase in $[K^+]_{o,soma}$ which led to a transition from rest to tonic firing (marked as a black arrow 'I' in the first panel in **A**). Phase II corresponds to a slow increase in $[K^+]_{o,dend}$ which led to a transition from tonic firing to bursting (marked as a black arrow 'II' in the first and second panels in **A**). Phase III represents a period of increased $[Na^+]_{i,soma}$, $[Na^+]_{i,dend}$ and decreasing $[K^+]_{o,soma}$ and $[K^+]_{o,dend}$ which led to the termination of the SLE (represented by a black arrow 'III' with its tip in the yellow domain in the third panel in **A**). Phase IV corresponds to the postictal period with elevated $[Na^+]_i$ and a return of $[K^+]_{o,soma}$, $[K^+]_{o,dend}$ to their baseline values (marked as a black arrow 'IV' in the third panel in **A**).

Figure 5. A comparison of the model without and with chloride accumulation. The six panels in each column show respectively (from top to bottom): the LFP signal, the PY cell membrane potential, the IN membrane potential, the extracellular potassium concentration and intracellular chloride concentration, the chloride and potassium KCC2 currents in the somatic compartments and the GABAa synaptic currents (Cl^- and HCO_3-) together with the leak chloride current. Additionally, the equilibrium potential of chloride and GABAa are shown in the second panel from the top. **(A)** When the $[Cl^-]_i$ accumulation mechanism was blocked, the chloride concentration was fixed at the reference value (fourth panel, blue). Without chloride accumulation, the PY cell (second panel) fired tonic train of spikes due to transient rise in $[K^+]_o$ (fourth panel, red) mediated by the IN discharge triggered by the current injection (yellow, third panel). Elevated $[K^+]_o$ and fixed $[Cl^-]_i$ promoted K^+ influx via KCC2 (fifth panel, red), thus lowering $[K^+]_o$ and further preventing the generation of the full SLE. **(B)** With chloride accumulation, the IN discharge led to an increase in E_{Cl} and E_{GABAa} (second panel, blue and light blue) which reduced the hyperpolarizing $I_{Cl,leak}$ and I_{GABAa} currents and enhanced excitability.

1510 The increase in firing rate of the PY cells led to prolonged $[K^+]_o$ accumulation (fourth panel, red)
1511 leading to the full SLE.

1512 **Figure 6. The evolution of inter-burst intervals (IBI) in the model and experimental data.**
1513 **(A)** In the simulation, the background input was removed and compensated with a small
1514 depolarizing current injected into the PY cells to preserve the duration of the SLE. A decreasing
1515 rate of bursting is visible in the LPF signal and in the detected bursts marked above the trace (top
1516 panel). The evolution of the IBI is shown with the y-axis on a linear scale (middle panel) and a
1517 log scale (bottom). On a linear y-axis plot, the data appear curved while on a semi-log plot they
1518 lay on a straight line, suggesting exponential scaling of the IBI with time. The red line in each
1519 plot represents the best fit for the detected IBI; linear function (middle panel) and exponential
1520 function providing a linear relationship on a semi-log plot (bottom panel). The root mean square
1521 error (RMSE) between the data points and fitted function is shown in each window. The
1522 exponential function fit yielded a smaller RMSE compared to the linear, logarithmic or square
1523 root fits (see Methods), providing quantitative confirmation that at the end of the simulated SLE,
1524 the IBI duration increased exponentially with time. **(B)** The evolution of the IBI during the SLE
1525 induced by application of bicuculline in the whole-brain *in vitro* preparation (Boido et al., 2014;
1526 Gnatkovsky et al., 2008). **(C)** IBI evolution during a seizure recorded with intracerebral
1527 electrodes positioned in the temporal lobe in a patient submitted to presurgical evaluation
1528 (courtesy of Laura Tassi, Epilepsy Surgery Center, Niguarda Hospital, Milano, Italy). In **B** and
1529 **C**, the detected IBI lay on a straight line on the semi-log plot and the exponential fit resulted in
1530 a smaller RMSE compared to the linear, logarithmic or square root fits, validating the model
1531 prediction of an exponential increase in the IBI at the end of a seizure. Only linear and
1532 exponential fits are shown. The results for all considered fits are provided in Figure 6 – source
1533 data 1.

1534 **Figure 6 – supplementary figure 1. Inter-burst interval slowing mediated by ion**
1535 **concentration changes.** The SLE was simulated by variations in K^+, Na^+ and Cl^- concentrations.
1536 For the first 50 seconds ion concentrations varied as in Figure 4B. Afterwards, the concentration
1537 of only one ion type was varied, while concentrations of all other ions were held constant. **(A)**
1538 In the bursting phase, discharges of PY cells were synchronous and the network dynamics was
1539 well captured by the membrane potential of a single PY cell, shown in the top panel. After second
1540 50, a linear decrease in $[K^+]_o$ (second panel) and constant $[Na^+]_i$ and $[Cl^-]_i$ (third and fourth panel,
1541 respectively) led to IBI slowing and SLE termination. The detected bursts are marked above the

trace. Blue bars mark analyzed IBI epoch. Four bottom panels show evolution of IBI (black points) fitted with linear, exponential, square root and logarithmic functions (red lines, see Methods), as marked on the left of the figure. The root mean square error (RMSE) between the data points and fitted function is shown in each window. Among all four fits, exponential fit marked by blue rectangle, provided the lowest RMSE. **(B)** Linear increase in $[Na^+]_i$ or **(C)** linear decrease in $[Cl^-]_i$ led to logarithmic IBI scaling (blue rectangle).

Figure 7. An analysis of network excitability in the postictal period. In this figure, the background input was removed from the simulation and compensated with a small depolarizing current injected into the PY cells, as in Figure 6. **(A)** The LFP signal. **(B)** The PY cell membrane potential with external periodic stimulation delivered every 5 seconds, marked by the arrows (violet, stim.). The amplitude of the stimulation was set at just above the threshold for triggering a spike in the interictal period. **(C)** The extracellular potassium in the somatic and dendritic compartments. **(D** and **E)** The net Na^+/K^+-pump current in the somatic and dendritic compartment, respectively. The vertical broken line (blue) in all panels marks the SLE offset time without periodic stimulation. Immediately after termination of the SLE, the network was still excitable due to increased $[K^+]_o$. Shortly afterward, the excitability decreased due to an increased Na^+/K^+-pump current that outlasted the increase in $[K^+]_o$. Increased I_{pump} and decreased $[K^+]_o$ which occurred shortly after the termination of the SLE, led to a postictal period during which the network did not respond to external stimulation for approximately 90 seconds.

Appendix I figure legends

Appendix I - figure 1. A bifurcation diagram of a single PY cell. The 2D bifurcation diagram demonstrates the behavior of a single PY cell as a function of extracellular potassium concentration in the dendritic ($[K^+]_{o,dend}$) and somatic compartments ($[K^+]_{o,soma}$) used as control parameters. Concentrations of all other ions were fixed at their reference values (except chloride: $[Cl^-]_{i,soma}$, $[Cl^-]_{i,dend}$ equal to 7 mM), all ion accumulation mechanisms were blocked and all synaptic connections were removed. **(A)** The three graphs show the PY cell activity traces for different values of the control parameters: resting (yellow, $[K^+]_{o,soma}$ = 3.5 mM, $[K^+]_{o,dend}$ = 3.5 mM), tonic firing (violet, $[K^+]_{o,soma}$ = 4.5 mM, $[K^+]_{o,dend}$ = 4 mM) and bursting (dark blue, $[K^+]_{o,soma}$ = 6.5 mM, $[K^+]_{o,dend}$ = 4 mM). In each panel, 2 seconds of activity is shown. **(B)** The colors of the 2D diagram correspond to the types of activity shown above in **(A)**. For low $[K^+]_{o,dend}$ and $[K^+]_{o,soma}$ the cell was at rest. A moderate increase in either $[K^+]_{o,dend}$ or $[K^+]_{o,soma}$,

or both, led to tonic firing. Subsequent increases in these parameters led to bursting.

Appendix I - figure 2. A comparison of tonic firing (A) and bursting (B) of a PY cell. In each column, the membrane potential of a cell (top) and the activation gate of I_{KM} (bottom) is shown. During tonic firing, the activation gate of the M-type potassium current was closed. The prolonged depolarization of the cell during bursting led to the opening of the activation gate *m* and activation of the I_{KM} current, which eventually terminated the burst. The simulation was performed using an isolated PY cell model with the concentrations of all ions fixed at their reference values, except $[Cl^-]_{i,soma}$= 7, $[Cl^-]_{i,dend}$ = 7 mM and **(A)**: $[K^+]_{o,soma}$ = 3.5 mM, $[K^+]_{o,dend}$ = 4.5 mM, **(B)**: $[K^+]_{o,soma}$ = 5.25 mM and $[K^+]_{o,dend}$ = 4.5 mM.

Appendix I - figure 3. A simulation of biphasic GABAa response. In this simulation size of both PY compartments was scaled down by factor 10, to represent small dendritic compartments. Single GABAa synapse was located in a segment having diameter 1.5 um and length 2 um (i.e., having volume 1000 times smaller and GABAa conductance density 100 times larger than soma in the original model). **(A)** High frequency IN firing (shown schematically by V_{IN}, yellow; not to scale) was induced by IN current stimulation of 100 ms duration. GABAa receptor-mediated postsynaptic potential response consisted of the initial hyperpolarization followed by a long-lasting depolarization (V_{PY}, black). Chloride accumulation (**(B)**, blue) was mediated by large Cl^- influx via GABAa receptor as compared to Cl^- extrusion via KCC2 (**(C)** vs. **(D)**). Accordingly, the biphasic potential resulted from positive shift in E_{Cl} (**(A)**, blue) and relatively high E_{HCO3} (**(A)**, violet) leading to depolarizing shift in E_{GABAa} (**(A),** light blue). During GABAa receptor activation V_{PY} was clamped to E_{GABAa} due to large GABAa conductance density.

Appendix I - figure 4. Volume changes during an SLE in the model. The panels show from top to bottom: LFP, relative volume changes and representative changes in intracellular A^- ion and extracellular Cl^- concentration in the PY somatic compartment during an SLE. $[A^-]_i$ was affected only by volume changes while $[Cl^-]_o$ was additionally affected by inward chloride leak and GABAa currents, KCC2 and Cl^- diffusion to the bath. It can be seen that an increase in intracellular space (IS) volume (second panel, dark blue) is exactly mirrored by a decrease in $[A^-]_i$. A decrease in extracellular space (ES) volume (third panel, violet) gives rise to an increase in $[Cl^-]_o$ above baseline despite Cl^- influx into the cells, in agreement with the experimental data (Dietzel et al., 1982).

Source data files

Figure 3 – source data 1

Source files for an SLE recordings in the *in vitro* isolated whole guinea pig brain

This zip archive contains experimental data shown in Figure 3. Seizure-like events were induced by 3-min arterial perfusion of 50 microM bicuculline and were recorded in the entorhinal cortex of the *in vitro* isolated whole guinea pig brain. The data are in the Matlab format (.mat). Matlab script (.m) loads the data from the file and creates the plot.

Figure 6 – source data 1

Source files for seizure data used in the analysis of inter-burst interval slowing.

This zip archive contains simulated and experimental data shown in Figure 6. The source data are in the Matlab format (.mat). Separate Matlab scripts (.m) are provided for the analysis of inter-burst interval distribution at the end of a seizure in the Model, Whole guinea pig brain and TLE patient. Each script loads the data, calculates linear, exponential, logarithmic and square root fits with root mean square error and creates the plots for each fit.

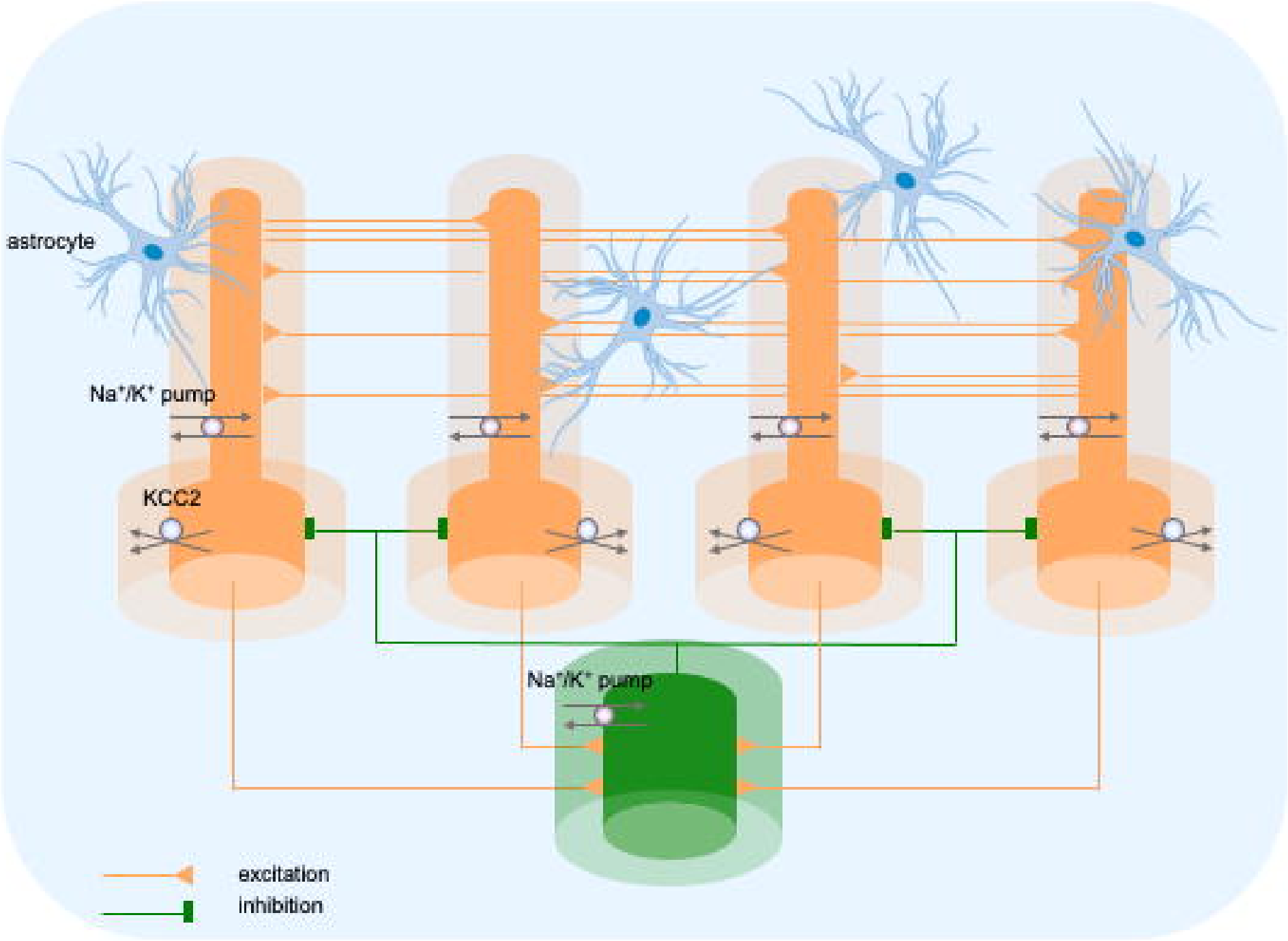
astrocyte
Na⁺/K⁺ pump
KCC2
Na⁺/K⁺ pump
excitation
inhibition

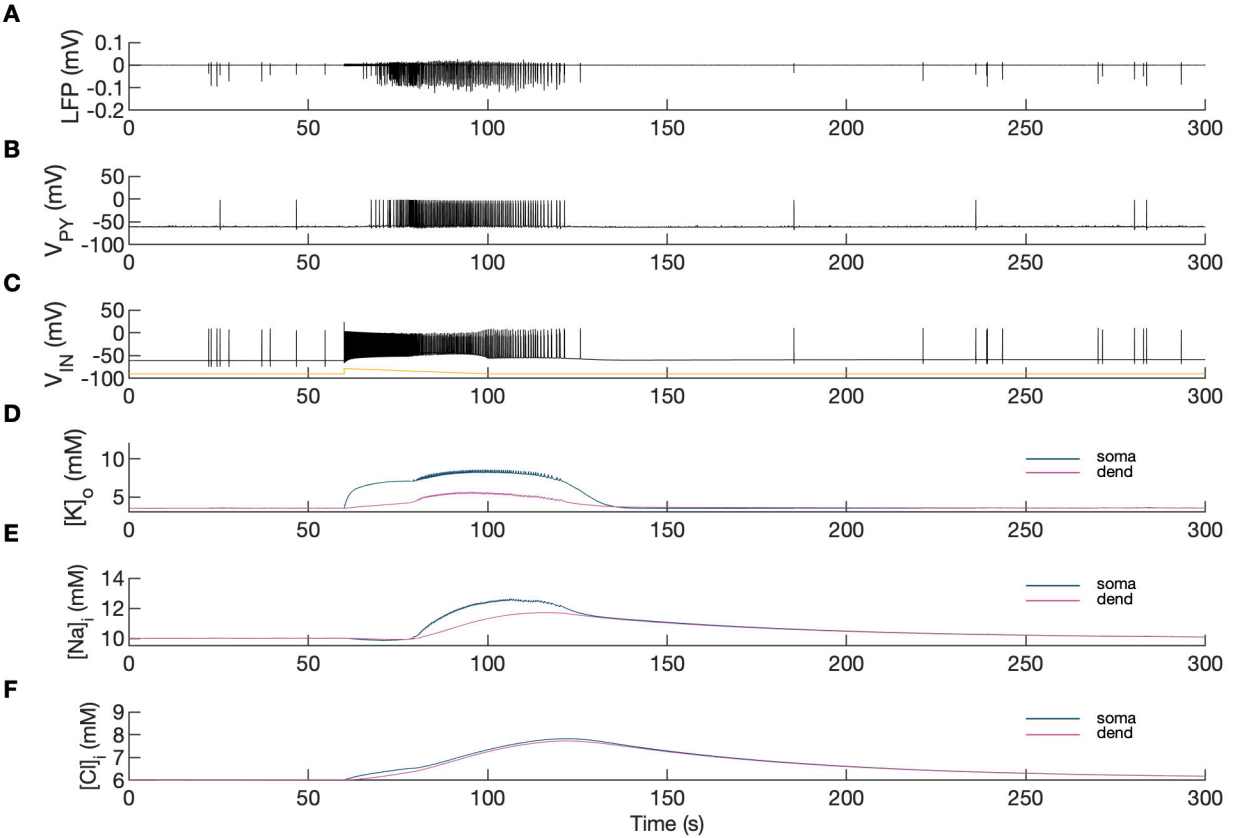
A
LFP (mV)
0.1
0
-0.1
-0.2
B
V_{PY} (mV)
50
0
-50
-100
C
V_{IN} (mV)
50
0
-50
-100
D
$[K]_o$ (mM)
10
5
soma
dend
E
$[Na]_i$ (mM)
14
12
10
soma
dend
F
$[Cl]_i$ (mM)
9
8
7
6
soma
dend
0
50
100
150
200
250
300
Time (s)

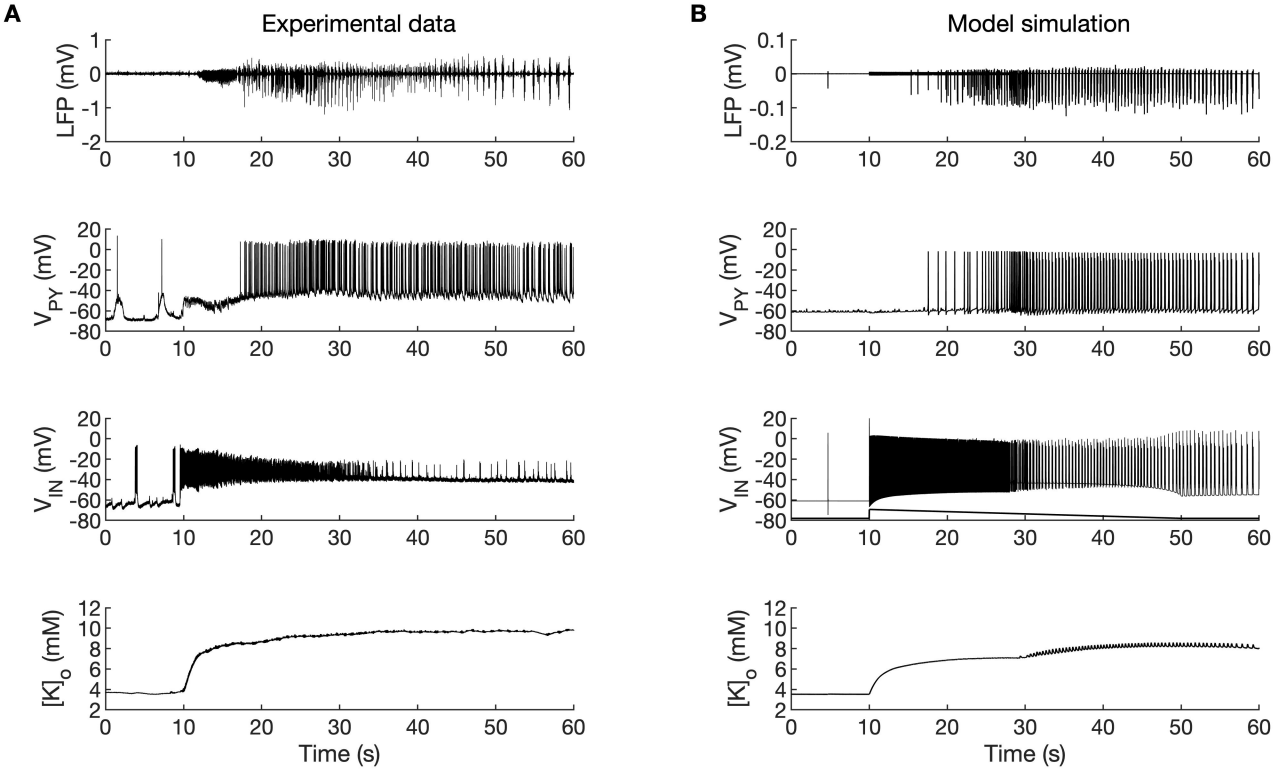
A
Experimental data
B
Model simulation
LFP (mV)
V_{PY} (mV)
V_{IN} (mV)
$[K]_o$ (mM)
Time (s)

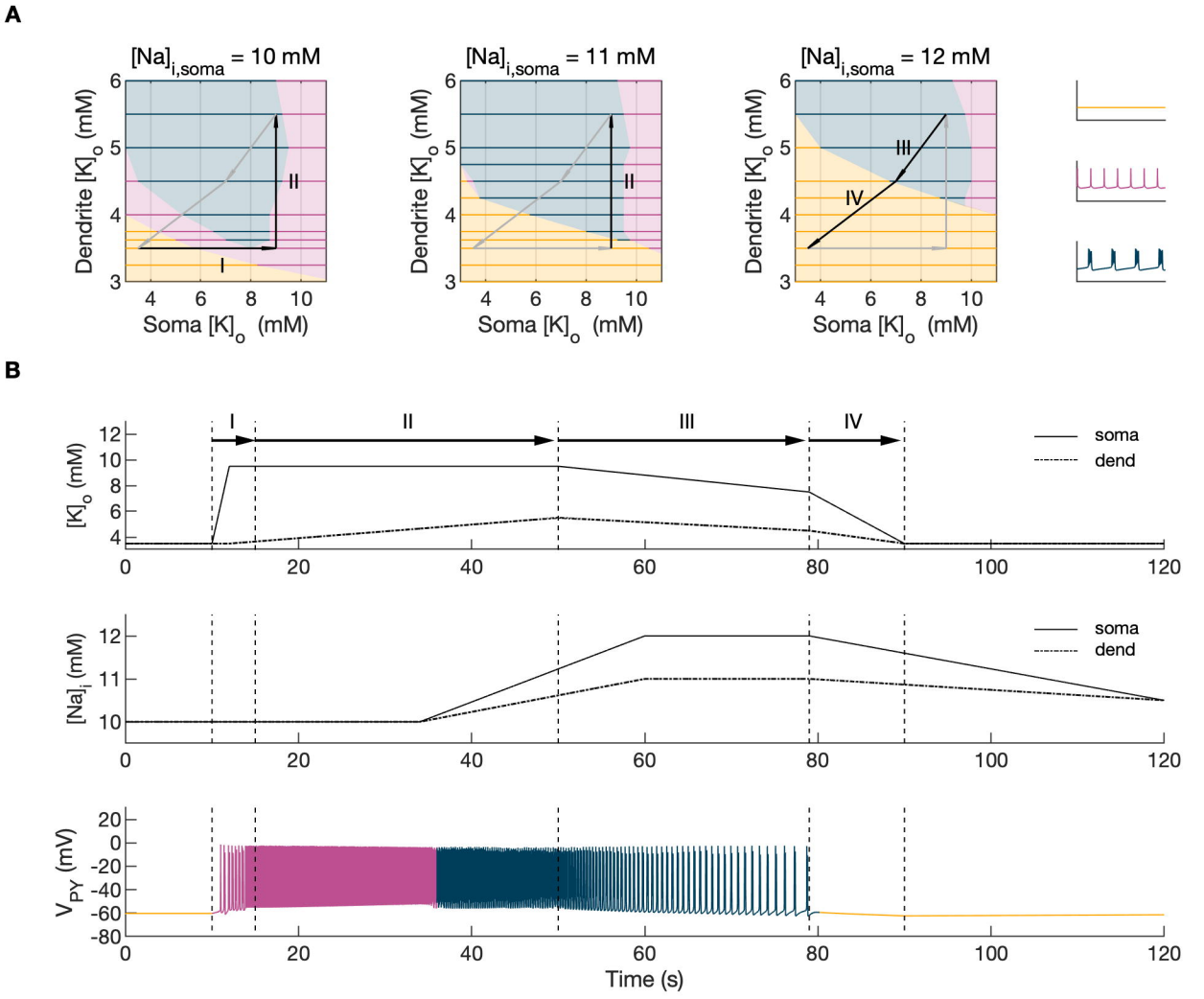
A
[Na]i,soma = 10 mM
[Na]i,soma = 11 mM
[Na]i,soma = 12 mM
Dendrite [K]o (mM)
Soma [K]o (mM)
I
II
III
IV
B
[K]o (mM)
[Na]i (mM)
VPY (mV)
Time (s)
soma
dend

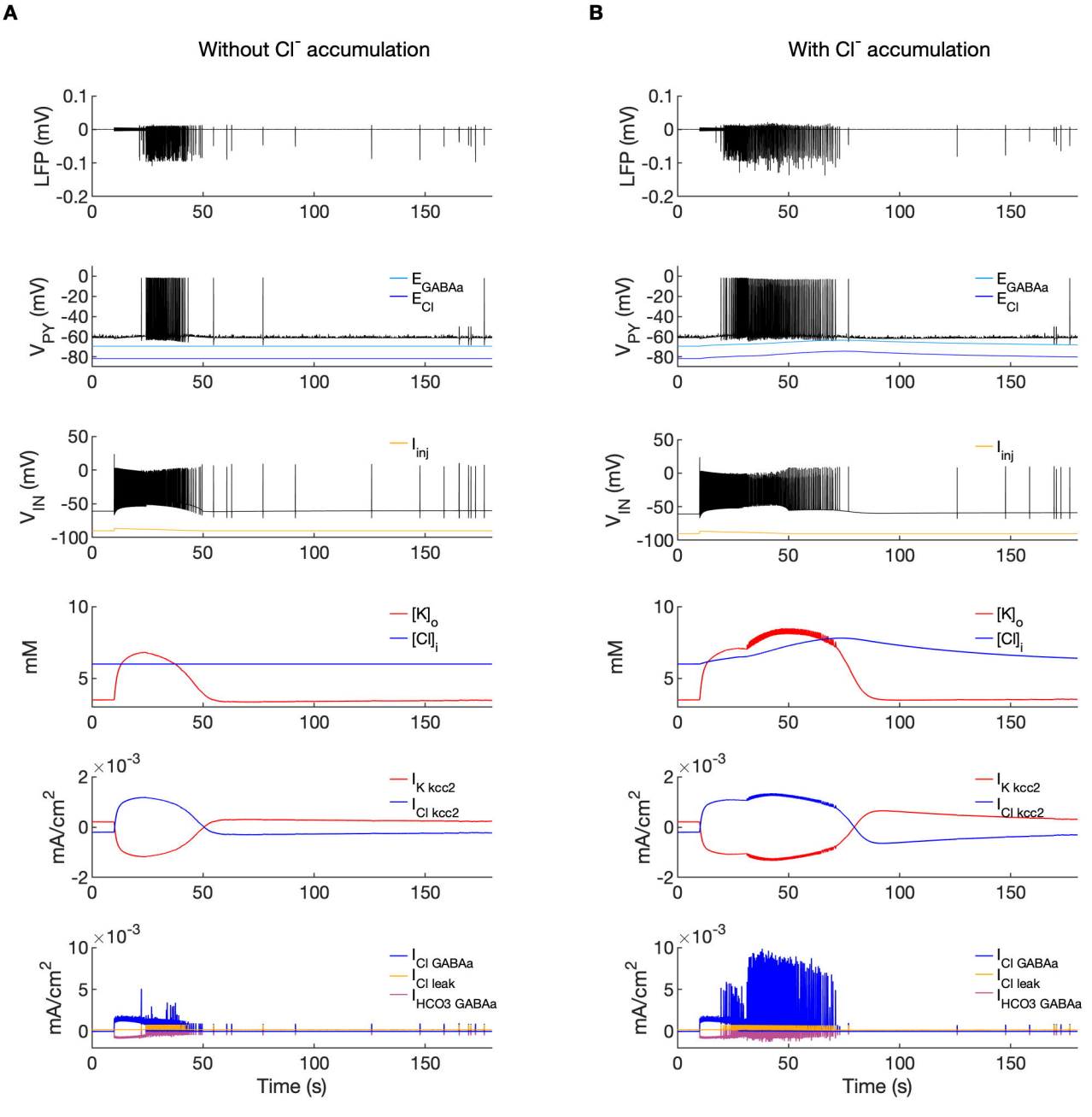
A
Without Cl⁻ accumulation
B
With Cl⁻ accumulation
LFP (mV)
V_PY (mV)
V_IN (mV)
mM
mA/cm²
×10⁻³
E_GABAa
E_Cl
I_inj
[K]_o
[Cl]_i
I_K kcc2
I_Cl kcc2
I_Cl GABAa
I_Cl leak
I_HCO3 GABAa
Time (s)

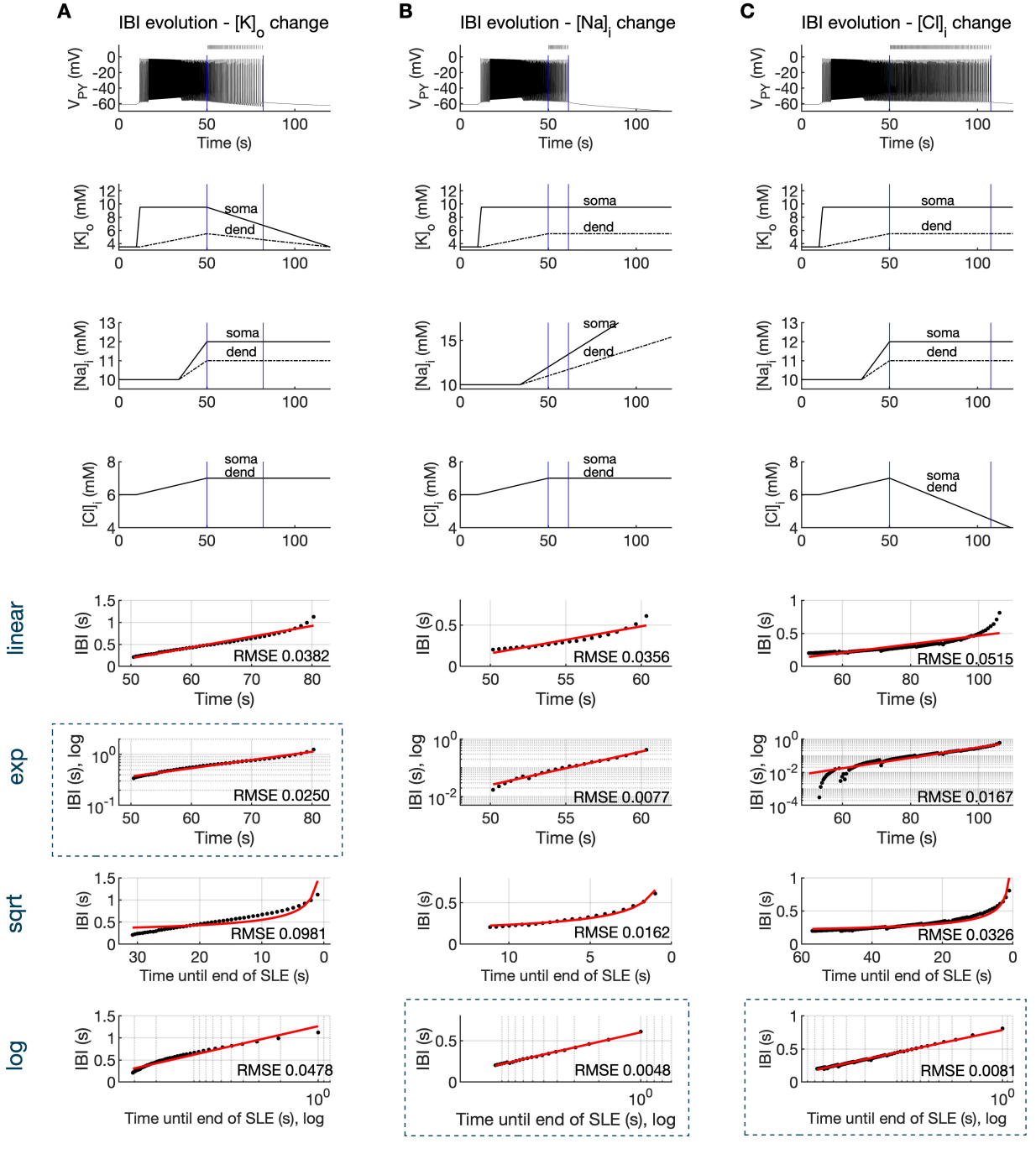
A
IBI evolution - [K]o change
B
IBI evolution - [Na]i change
C
IBI evolution - [Cl]i change
VPY (mV)
Time (s)
[K]o (mM)
[Na]i (mM)
[Cl]i (mM)
soma
dend
linear
exp
sqrt
log
IBI (s)
IBI (s), log
Time (s)
Time until end of SLE (s)
Time until end of SLE (s), log
RMSE 0.0382
RMSE 0.0356
RMSE 0.0515
RMSE 0.0250
RMSE 0.0077
RMSE 0.0167
RMSE 0.0981
RMSE 0.0162
RMSE 0.0326
RMSE 0.0478
RMSE 0.0048
RMSE 0.0081

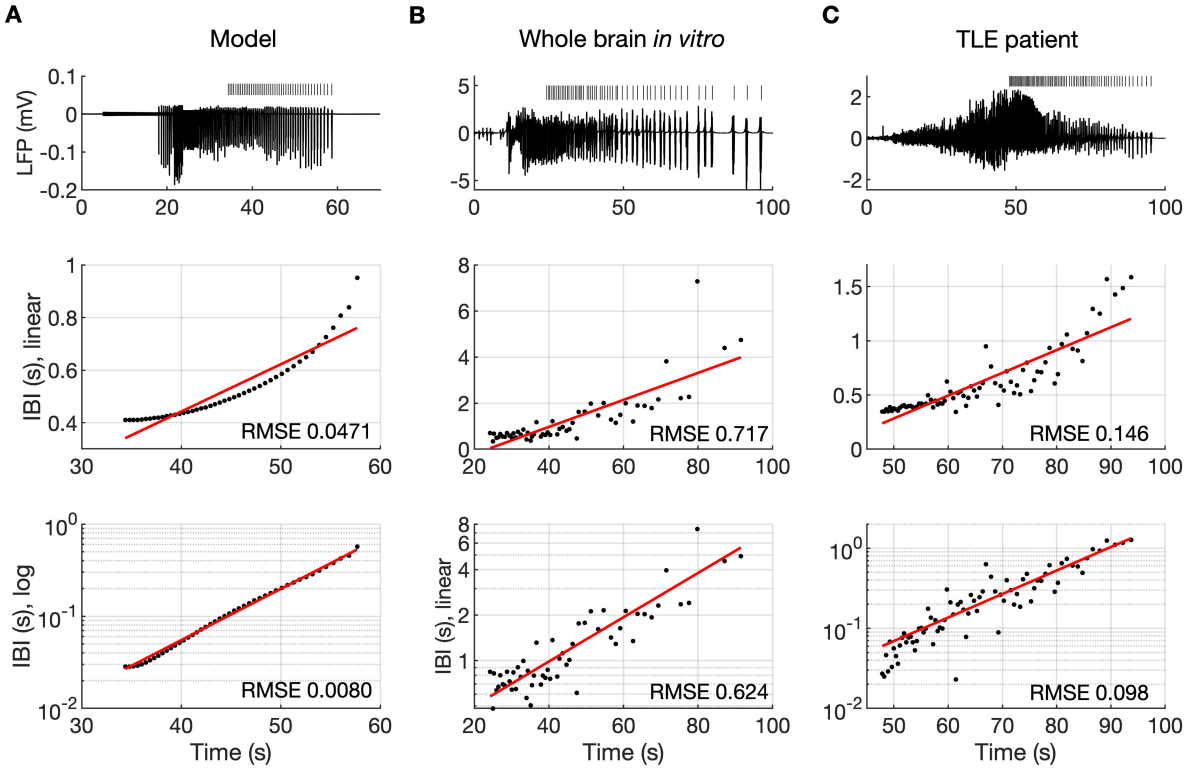
A
Model
B
Whole brain in vitro
C
TLE patient
LFP (mV)
IBI (s), linear
IBI (s), log
RMSE 0.0471
RMSE 0.717
RMSE 0.146
RMSE 0.0080
RMSE 0.624
RMSE 0.098
Time (s)

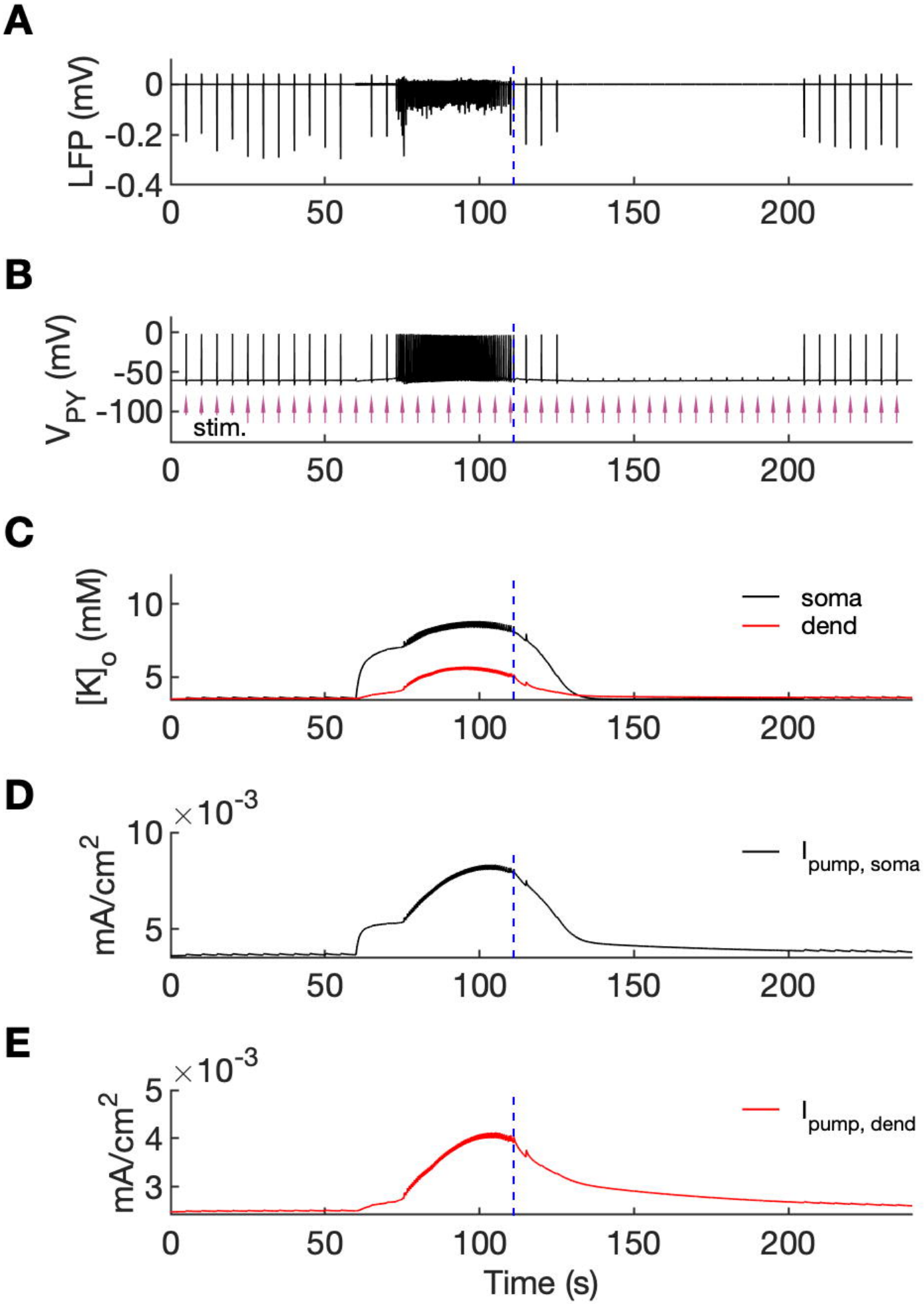
A
LFP (mV)
0
-0.2
-0.4
0
50
100
150
200
B
V_{PY} (mV)
0
-50
-100
stim.
0
50
100
150
200
C
$[K]_o$ (mM)
10
5
soma
dend
0
50
100
150
200
D
mA/cm^2
$\times 10^{-3}$
10
5
$I_{pump, soma}$
0
50
100
150
200
E
mA/cm^2
$\times 10^{-3}$
5
4
3
$I_{pump, dend}$
0
50
100
150
200
Time (s)

A

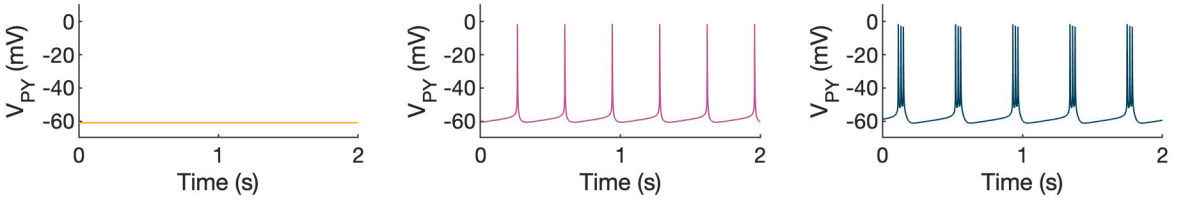
V_{PY} (mV)
0
-20
-40
-60
0
1
2
Time (s)

B

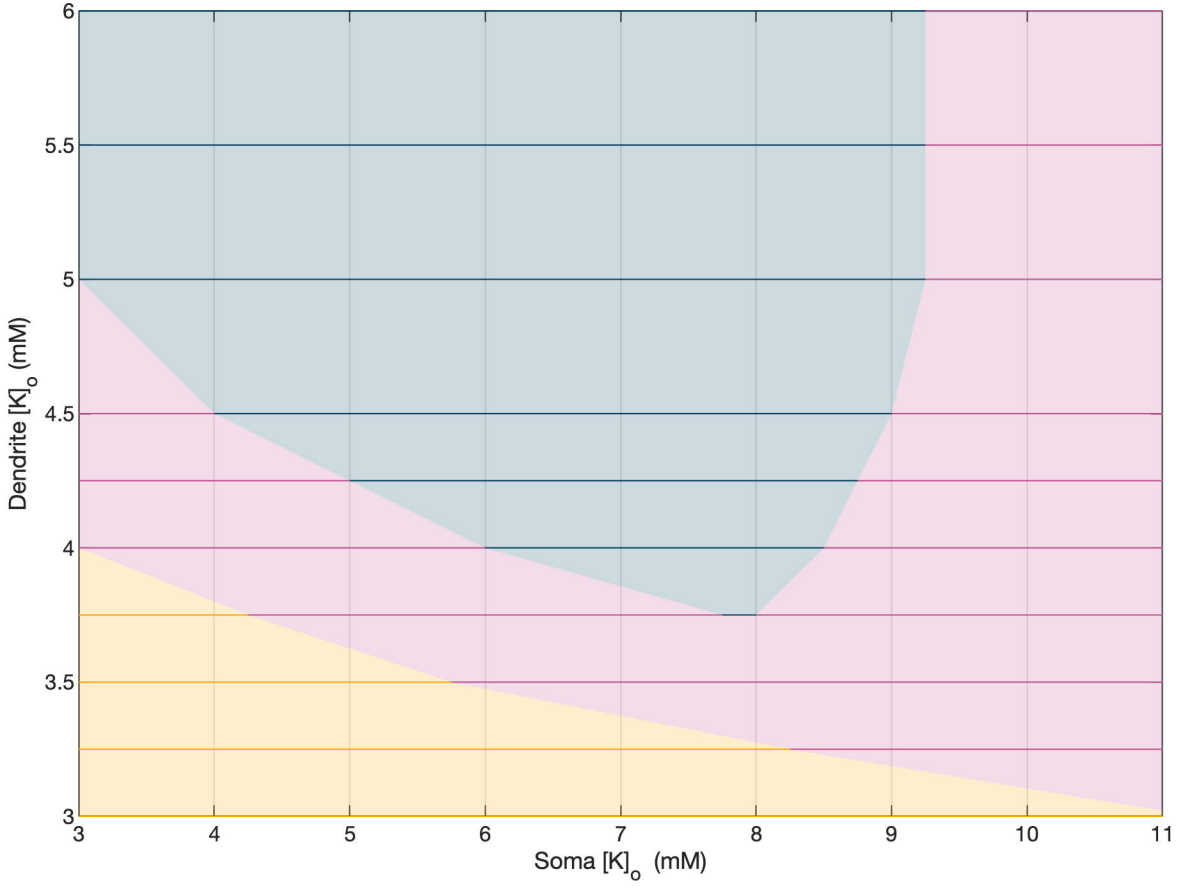
Dendrite $[K]_o$ (mM)
6
5.5
5
4.5
4
3.5
3
3
4
5
6
7
8
9
10
11
Soma $[K]_o$ (mM)

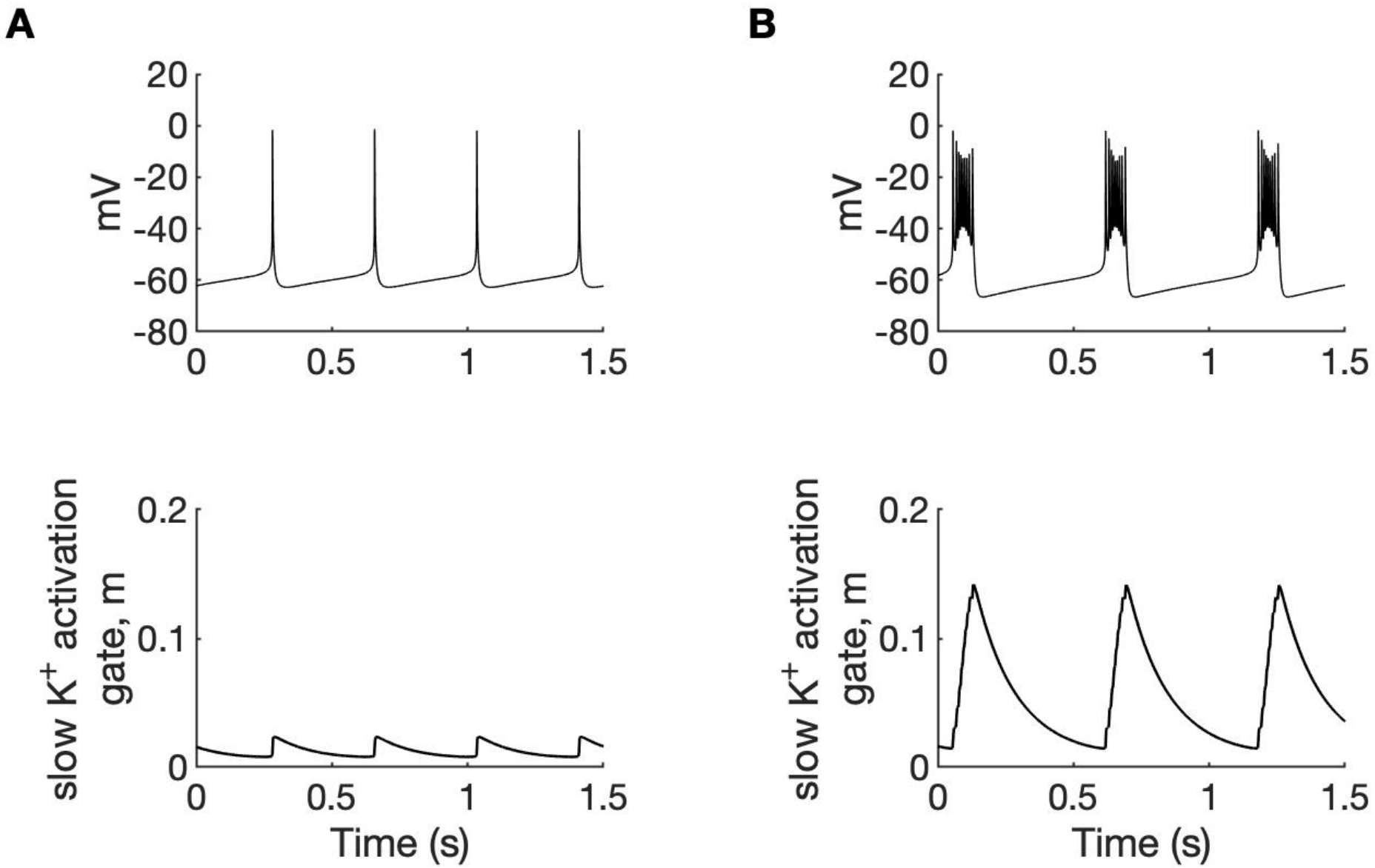
A
B
20
0
-20
-40
-60
-80
mV
0
0.5
1
1.5
0.2
0.1
0
slow K+ activation gate, m
Time (s)

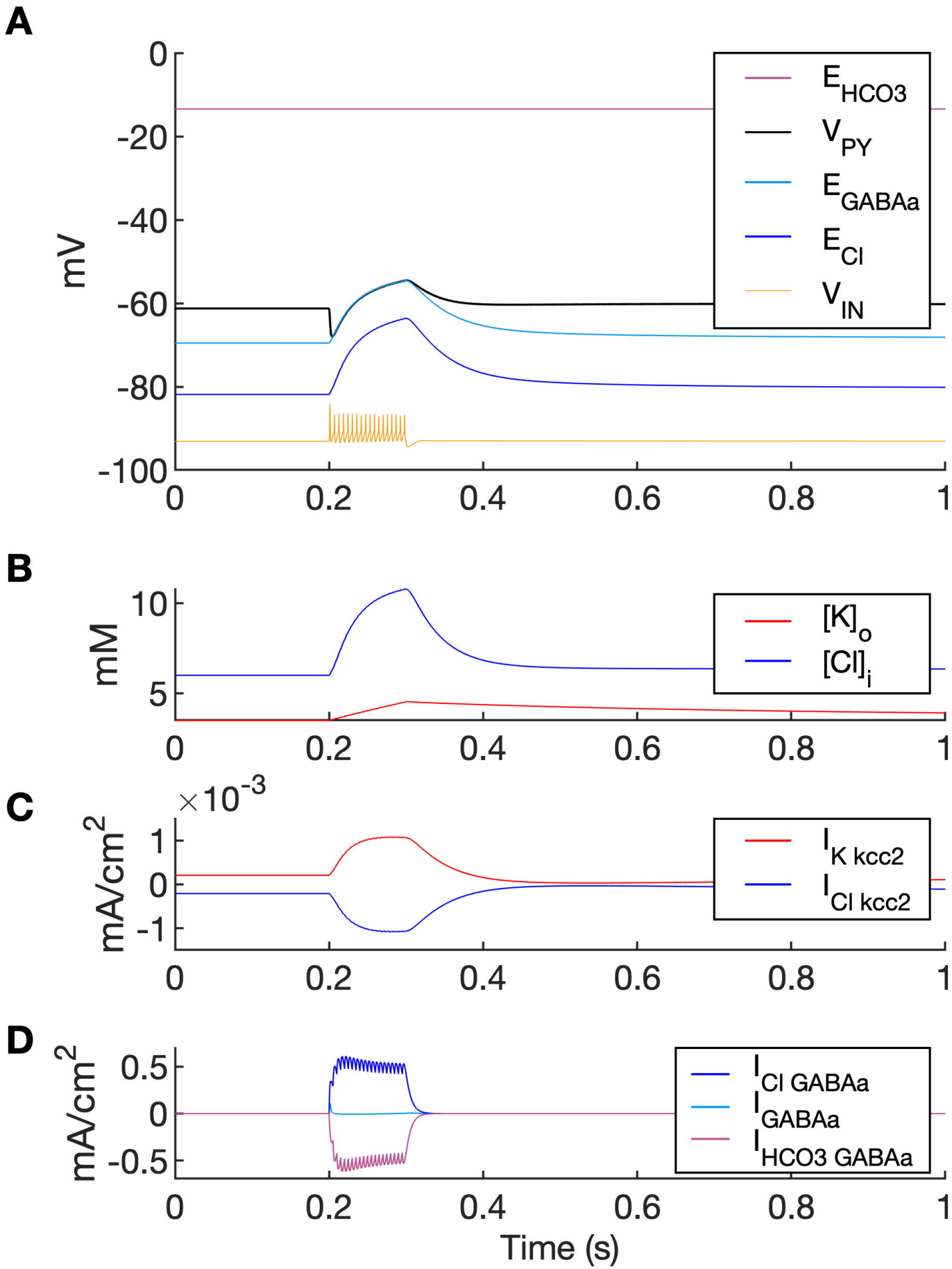
A
0
-20
-40
-60
-80
-100
mV
0
0.2
0.4
0.6
0.8
1
E HCO3
V PY
E GABAa
E Cl
V IN
B
10
5
mM
[K] o
[Cl] i
C
×10-3
1
0
-1
mA/cm2
I K kcc2
I Cl kcc2
D
0.5
0
-0.5
mA/cm2
I Cl GABAa
I GABAa
I HCO3 GABAa
Time (s)

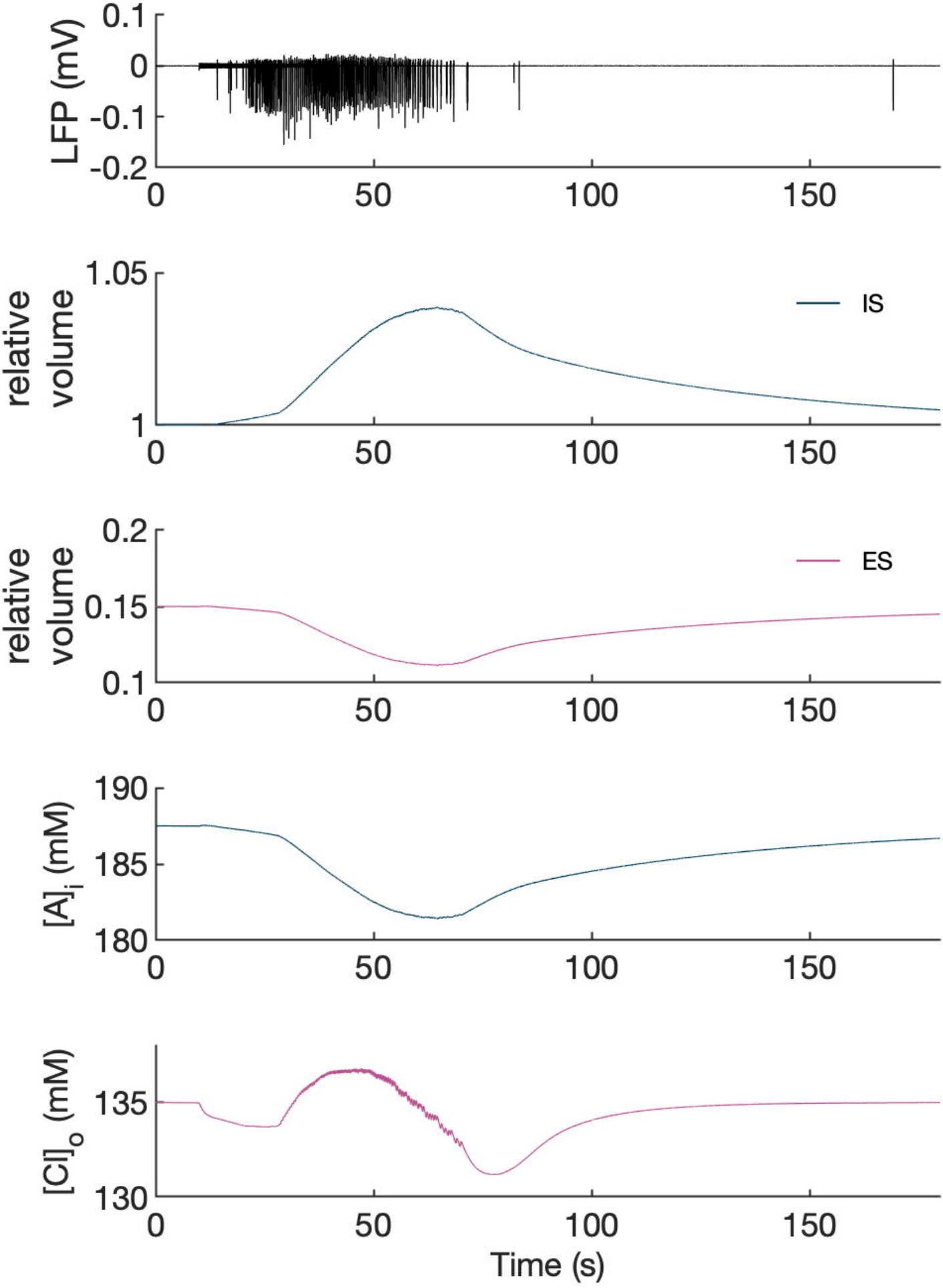
LFP (mV)
0.1
0
-0.1
-0.2
0
50
100
150
relative volume
1.05
1
IS
relative volume
0.2
0.15
0.1
ES
[A]i (mM)
190
185
180
[Cl]o (mM)
135
130
Time (s)